Chemie der Erde 77 (2017) 281–302

Contents lists available at ScienceDirect

Chemie der Erde

journal homepage: www.elsevier.de/chemer

Geochemistry and petrogenesis of Kolah-Ghazi granitoids of Iran: Insights into the Jurassic Sanandaj-Sirjan magmatic arc

Marzieh Bayati[a], Dariush Esmaeily[a,*], Reza Maghdour-Mashhour[b], Xian-Hua Li[c], Robert J. Stern[d]

[a] Department of Geology, Faculty of Science, University of Tehran, Tehran 14155-64155, Iran
[b] School of Geosciences, Faculty of Science, University of the Witwatersrand, Johannesburg, South Africa
[c] State Key Laboratory of Lithospheric Evolution, Institute of Geology and Geophysics, Chinese Academy of Sciences, Beijing 100029, China
[d] Geosciences Department, University of Texas at Dallas, Richardson, TX 75083-0688, USA

ARTICLE INFO

Article history:
Received 17 January 2017
Accepted 27 February 2017
Editorial handling - Hadi Shafaii Moghadam

Keywords:
Zircon U–Pb dating
Jurassic magmatism
S-type granite
Neo- Tethys
Sanandaj Sirjan zone

ABSTRACT

Kolah-Ghazi granitoid (KGG), situated in the southern part of the Sanandaj–Sirjan Zone (SNSZ), Iran, is a peraluminous, high K calc-alkaline, cordierite-bearing S-type body that is mainly composed of monzogranite, granodorite and syenogranite. Zircon U–Pb ages indicate that the crystallization of the main body occurred from 175 Ma to 167 Ma. Two kinds of xenoliths are found in KKG rocks: (i) xenoliths of partially melted pelites including cordierite xenocrysts and aluminoslicates, and (ii) mafic microgranular enclaves that reflect the input of mantle-derived mafic magmas. Field observations and geochemical data of KGG rocks are consistent with their derivation from a multiple sources including melts of metasediments and mantle-derived melts. We infer that these magmas originated by the anatexis of a metasedimentary source (mixture of metapelite and metagreywacke) in the mid- to lower-crust under low water-vapor pressures (0.5-1 Kbar) and temperature of ~800 °C. KGG is the product of biotite incongruent melting of this metasedimentary source. S-type granites are commonly thought to be produced in continent-continent collision tectonic environment. However, trace element discrimination diagrams show that S-type KGG rocks formed in an arc-related environment. The roll-back of Neo- Tethyan subducting slab accompanying oblique subduction in Late Triassic to Early Jurassic time induced trench rollback, back arc basin opening and filling with turbidite flysch and molasse- type siliciclastic sediments of the Shemshak Group on the overriding plate. Further changes in the subducting slab to flat subduction in Middle Jurassic time, the time of peak magmatism in the SNSZ, led to thickening and high temperature-low pressure metamorphism of the backarc turbidite deposits and consequent anatexis of the metasedimentary source to produce the KGG S- type rocks along with several other I-type granitoids in the SNSZ.

1. Introduction

The Iranian sector of the Alpine-Himalayan orogenic belt is a complex assemblage of several aggregated and welded continental blocks with different stratigraphic and tectonic histories separated by narrow belts of Late Cretaceous ophiolites such as Nain-Baft, Nayriz and Sabzevar (Aghanabati, 2004; Ghazi et al., 2004; Berberian and King, 1981). Middle Mesozoic to late Cenozoic magmatic rocks were generated during Neo-Tethyan subduction beneath the Iranian blocks (Verdel et al., 2011). There are two NW-SE trending magmatic belts parallel to the Neo-Tethyan suture zone in Iran; 1) the Sanandaj–Sirjan zone (SNSZ) which is dominated by Jurassic–Cretaceous granitic plutons and minor volcanic rocks (Azizi and Moinevaziri, 2009) and 2) the Urumieh–Dokhtar Magmatic Belt (UDMB), of Late Cretaceous to Quaternary age (Berberian and King, 1981).

The SNSZ is a key tectonic element and is located close to the northeastern margin of the Zagros orogen (Mohajjel et al., 2003). Lithological and structural evidence indicates that the SNSZ experienced different geodynamic settings during its evolution by rifting from the Zagros basin with basic magmatism in Paleozoic time (i.e. opening of the Neo-Tethyan Ocean; Berberian and King, 1981) to an Andean type margin in Jurassic time (Alirezaei and Hassanzadeh, 2012; Alavi, 1994; Sheikholeslami et al., 2008; Fazlnia et al., 2009; Mohajjel et al., 2003). This was succeeded by formation of Late Cretaceous ophiolites of the Inner and Outer Zagros ophiolite belts

* Corresponding author.
E-mail address: esmaili@khayam.ut.ac.ir (D. Esmaeily).

http://dx.doi.org/10.1016/j.chemer.2017.02.003
0009-2819/

(Shafaii Moghadam and Stern, 2015). These ophiolite belts mark the SNSZ from Central Iran (Berberian and King, 1981; Mohajjel and Fergusson, 2000; Mohajjel et al., 2003; Davoudzadeh and Schmidt, 1984; Shafaii Moghadam et al., 2009). The subduction of Neo-Tethyan is considered to have been responsible for extensive arc magmatism from Early Jurassic to Cenozoic in the SNSZ (Mesozoic arc) and UDMB (Tertiary arc) (Alavi, 1994; Berberian and King, 1981; Omrani et al., 2008; Verdel et al., 2011; Aghazadeh and Mogaddam, 2010; Baharifar, 2004; Ghasemi and Talbot, 2006; Mohajjel et al., 2003; Chiou et al., 2013).

The first stage of subduction-related magmatism in Iran was during Jurassic time with peak activity at ~165 Ma, as evidenced by the presence of widespread volcanic and intrusive massifs that range in age from 199 to 144 Ma in the SNSZ (Chiou et al., 2013). Jurassic arc igneous activity is best preserved in the SNSZ. The main Jurassic intrusive bodies in the SNSZ include Azna (Moazzen et al., 2004; Sepahi and Athari, 2006), Aligudarz (Bagherian and Khakzad, 2001), Saqqez (Sepahi and Athari, 2006), Golpayegan (Davoudian et al., 2007) Hamadan (Sepahi, 1999) Kolah-Ghazi (Noghreyan and Tabatabaei-Manesh, 1995; Khalili and Khalili, 2002), Borujerd and Astaneh (Masoudi, 1997; Ahmadi Khalaji et al., 2007) (Fig. 1b).

The Kolah-Ghazi granitoid (KGG) and other SNSZ intrusions are associated with nearby Shahr-e-Kord high pressure metabasites, amphibolites and eclogites with mid-ocean ridge (MORB)-like compositions attributed to exhumed remnants of Neo-Tethyan oceanic lithosphere (Davoudian et al., 2006, 2007). These together with the proximity of the KGG to the Nain-Baft ophiolitic belt and the geochemical or geochronological similarity of the KGG to several other arc-related I-type granitoids in the SNSZ, make it important to better understand the KGG and what it tells us about SNSZ geodynamic evolution. Despite its significance, the age, geochemistry and geodynamics of the KGG remain poorly understood. Thus, a detailed study of this intrusion provides a unique opportunity to better understand Jurassic subduction and arc magmatism processes that took place beneath SW Eurasia. In this study, we present a detailed account of the field relations, rock types, mineral chemistry, whole-rock geochemistry, and SIMS zircon U-Pb dating of the KGG for the first time and use these data to determine the petrogenesis, source region and tectonic setting in the framework of Jurassic arc magmatism along the northern margins of Neo-Tethyan in the SNSZ.

2. Geological setting and field relationship

The SNSZ can be subdivided into two parts: (1) the southern part, deformed and metamorphosed in Middle to Late Triassic time; and (2) the northwestern part, deformed in Late Cretaceous time, which contains many intrusive felsic rocks of mainly Late Cretaceous–Paleocene age (Eftekharnejad, 1981; Rachidnejad-Omran, 2002; Ghasemi and Talbot, 2006; Shafaii Moghadam and Stern, 2011). The southern SNSZ is subdivided transversally into two separate parts with different tectonic histories: (i) Esfahan–Sirjan region in the north consisting of Paleozoic, Mesozoic, and Cenozoic sedimentary rocks with typical Central Iranian stratigraphies; and (ii) southwestern part (Shahrekord–Dehsard Terrane), which is an intensely faulted zone consisting of high to low grade metamorphic rocks and metasedimentary strata with intercalations of intermediate and basic volcanic rocks (Arfania and Shahriari, 2009).

The KGG lies within the Esfahan–Sirjan Block (32°20′ N–51°55′ E) southeast of Esfahan city along the southern extension of the Kolah-Ghazi ranges (Fig. 1). The Kolah-Ghazi range is a fault bounded, NW–SE trending anticlinorium, characterized by a belt of Jurassic to Cretaceous sedimentary rocks 50 km long and 7 km wide. The KGG crops out in three small separate exposures in the Lagoor-e-bozorg and Soroushjoon valleys along the main northern and southern faults of the Kolah-Ghazi range. The Najafabad–Kolah-Ghazi and Golpayegan faults restrict the northern and southern Kolah-Ghazi range, respectively, and are the main structural elements of the study area. These faults were active during Jurassic and Cretaceous time and their vertical movement formed large NW-SE oriented, fault- bounded basins in which Mesozoic sediment was deposited (Khosrow-Tehrani, 1970). The Jurassic succession in the Kolah-Ghazi region is dominated by shale and sandstone with interlayered fossil-bearing limestones (Zahedi, 1976). The Cretaceous sequence consists of Barremian to Coniacian basal conglomerate, sandstone, shale and limestone that unconformably overlies the KGG (Khosrow-Tehrani, 1970; Fig. 3). The presence of KGG clasts in the basal conglomerate of the overlying Cretaceous succession and contact metamorphism and hydrothermal alteration of Jurassic units testify to the KGG emplacement during Late Jurassic, before deposition of Early Cretaceous limestones.

The KGG is mainly composed of monzogranite, granodiorite and syenogranite associated with aplitic dykes and quartz-tourmaline veins (Fig. 2). It intruded the Jurassic shale, producing a narrow contact metamorphic aureole made of biotite-hornfels. Up to 10 cm oval xenoliths, both mafic microgranular enclaves (MMEs) and surmicaceous (biotite-aluminosilicate) enclaves (Fig. 3e) have been identified in KGG rocks. The surmicaceous enclaves are rounded xenoliths composed of andalusite, cordierite, spinel, sillimanite, biotite, plagioclase and quartz. The MMEs are fine-grained with biotite, plagioclase, quartz, apatite, and zircon as dominant assemblage.

3. Petrography

Detailed mapping of the KGG (Fig. 2) reveal three main rock types, hereafter referred to as granodiorite, monzogranite, and syenogranite. Monzogranite outcrops throughout the Soroushjoon valley, east and west of the Lagoor-e-bozorg and Cheshmehneyzar area. They are coarse-grained with a granular texture. Mineral assemblages include quartz (40%) alkali feldspar (30–35%), plagioclase (25–35%), biotite (5–10%) and some primary muscovite. Zircon, apatite, andalusite, sillimanite are common accessory minerals (Fig. 4f). Large phenocrysts of quartz show undulatory extinction and have inclusions of biotite, alkali feldespar, plagioclase and apatite. Plagioclase (altered to sericite) and alkali feldspar occur as euhedral to subhedral crystals with polysynthetic twins and Carlsbad twins, respectively.

Granodiorites are second in abundance after monzogranites and crop out as low high hills that intrude Jurassic shales and are unconformably overlain by Cretaceous limestones (Fig. 3a & b). These rocks show medium to coarse-grained textures with a simple mineralogy (Fig. 4d): quartz (25–30%), plagioclase (30–40%), alkali feldspar (<20%) and biotite (10–20%). Apatite, zircon, silimanite and andalusite are common accessory minerals, with some muscovite and spinel. Quartz crystals occur as anhedral isolated grains with undulatory extinction. Plagioclase forms rectangular to subhedral laths, 1–2 mm or less in length that exhibit variable amounts of sericitisation and zoning (Fig. 4e). Biotite occurs as brown flakes, 1–2 mm in length, with a preferred orientation; these are mostly altered to chlorite, cordierite and/or titanite (Fig. 4f). Evidence that cordierite in KGG formed from biotite includes the lack of zoning in cordierite crystals and the occurrence of the cordierite with biotite, spinel and aluminosilicate according to the following reaction:

$$\text{Biotite} + \text{Aluminosilicate} \rightarrow \text{Cordierite} + \text{Spinel}$$

Syenogranites are less abundant than monzogranite and granodiorite. There are several aplite veins with syenogranitic composition that are located in the western part of Lagoor-e-bozorg; these are porphyritic with a weak alteration consisting

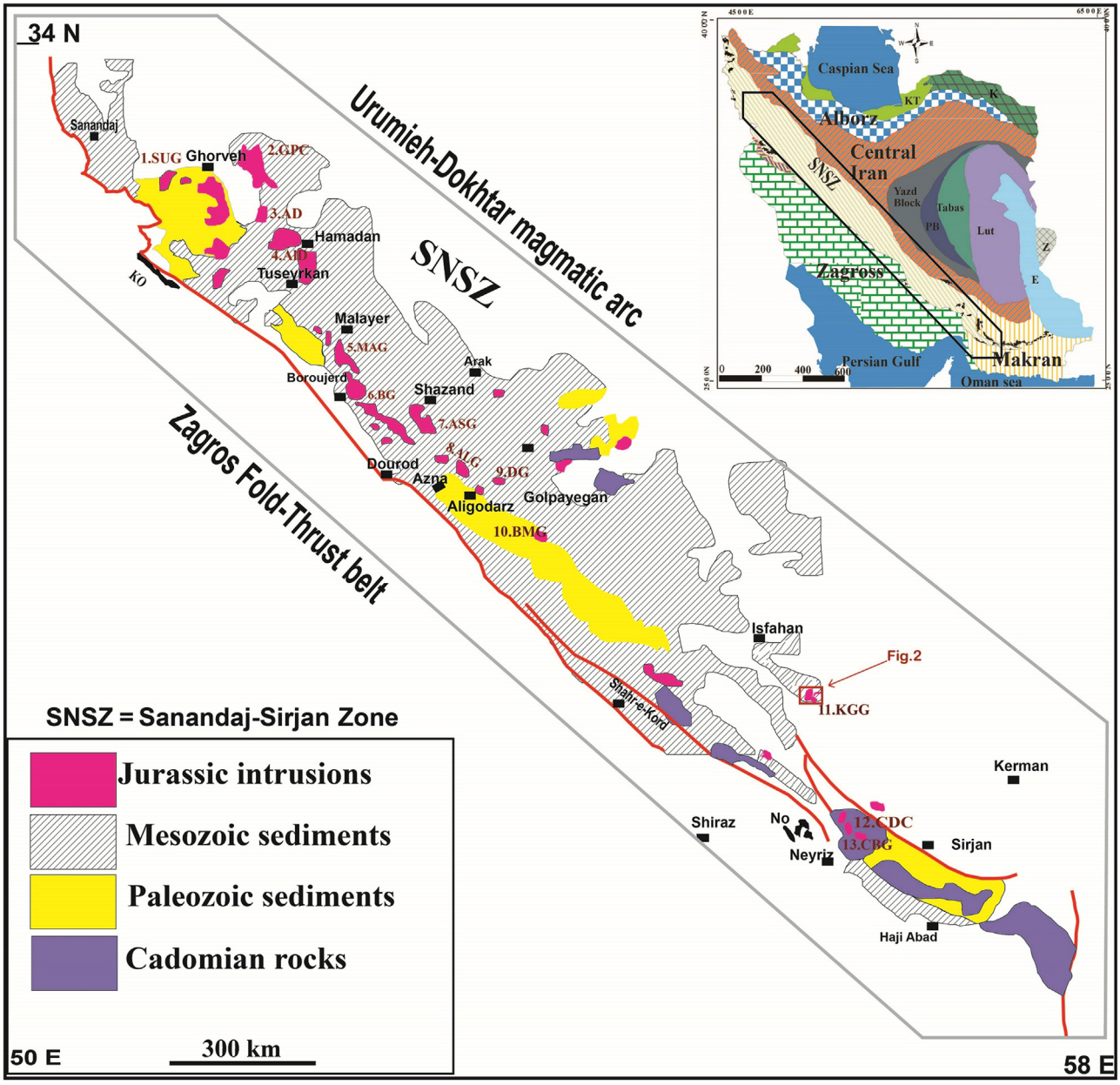

Fig. 1. Simplified geological map of the Sanandaj–Sirjan Zone (SNSZ) and its Jurassic plutons. Inset highlights the main tectonic features (based on Iran Structure map 1:2500000). SUG: Suffi abad granite; GPC: Ghorve plutonic complex; AD: Almagholagh diorite; ALD: Alvand batholiths; MAG: Malayer granitoids; BG: Borujerd granitoid; ASG: Astaneh granitoid; ALG: Aligudarz granitoid; DG: Dehbid granitoid; BMG: Bounin-Miyandasht granitoid; KGG: Kolah-Ghazi granitoid; CDC: Chah Dozdan batholith and Quri complex; CBG: Chah Bazargan gabbro; NO: Neyriz ophiolites and KO: Kermanshah ophiolites. The KGG is located at the south of SNSZ. References are shown in Table 9.

of sericite and chlorite. They are medium to coarse grained, with hypidiomorphic granular texture and contain abundant euhedral to subhedral phenocrysts of plagioclase (22–24 vol.%), K–feldspar (40–42%), and quartz (25–30%). These rocks are light in color and contain few mafic minerals. Subhedral to anhedral K–feldspars (0.5–2 mm) are usually perthitic. Quartz occurs in two generations; both as euhedral, early formed crystals and anhedral late stage grains. Magnetite, ilmenite, zircon, apatite ± titanite are the principal accessory minerals (Fig. 4h).

The surmicaceous enclaves exhibit granular texture with a weak alteration consisting of saussurite. They are anhedral to subhedral, dark in color and contain biotite, plagioclase, sillimanite, andalusite, cordierite, and spinel (Fig. 4i). Quartz occurs in matrix as anhedral late stage grains. White and Chappell (1977) reported similar assemblages in the mafic S-type granites of the Berridale and the northern parts of the Kosciuszko Batholith of Australia.

The MMEs are up to 50 cm but more commonly less than 20 cm in diameter. They are generally rounded and generally comprise the same minerals as the host rock, such as biotite, plagioclase, zircon, apatite and quartz, compared with which they are darker-colored, fine-grained and generally massive (Fig. 4j).

4. Analytical methods

4.1. Mineral major elements analyses

Major element compositions of KGG minerals were determined by JEOL wavelength dispersive electron probe X-ray microanalyzer (EPMA) using the JXA 8100 at the Institute of Geology and Geophysics, Chinese Academy of Sciences (IGG-CAS) (Beijing, China). Accelerating voltage, beam current, and beam diameter for

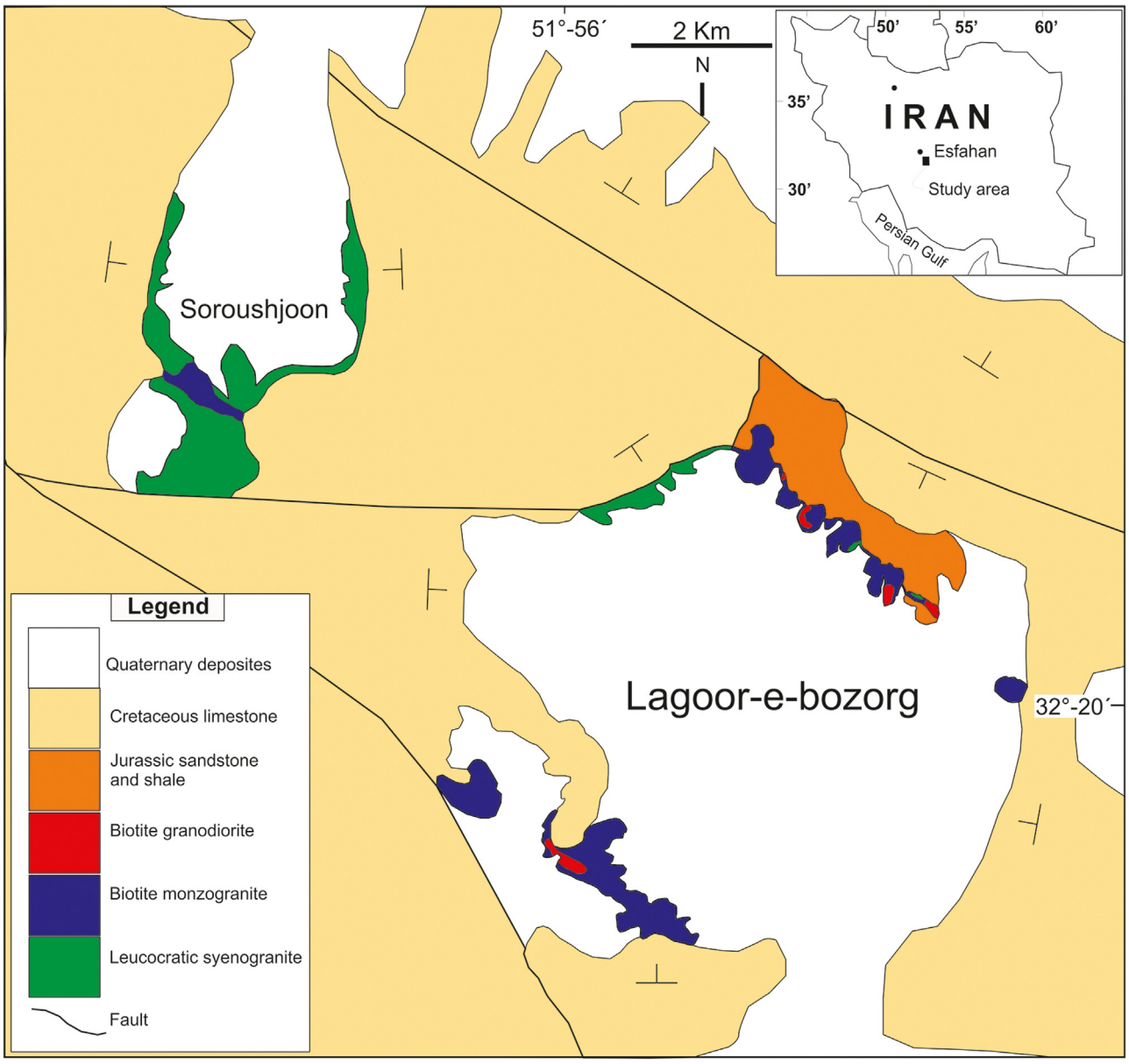

Fig. 2. Geological map of the Kolah-Ghazi region (modified after 1/100000 Shahreza geological map).

Table 1
Selected electron microprobe analyses (EPMA) of feldspar from granitoid rocks.

	Syenogranite					Monzogranite				Granodiorite			
SiO_2	55.81	59.005	59.725	56.610	55.516	54.091	54.224	56.686	55.139	56.295	57.056	56.067	56.169
TiO_2	0.037	0	0.025	0.011	0.002	0.037	0.011	0	0	0.022	0.017	0	0.033
Al_2O_3	27.097	25.721	25.691	27.597	27.758	29.055	28.789	27.013	28.172	27.669	27.696	27.928	27.585
FeO	0.066	0.025	0.048	0.047	0.06	0.029	0.018	0.032	0.034	0.022	0.002	0	0.028
MnO	0.032	0.007	0	0	0.007	0.03	0.02	0.009	0.01	0.023	0.023	0.043	0.029
MgO	0.006	0.006	0	0	0	0	0	0.002	0	0.003	0.005	0	0.003
CaO	8.591	7.048	6.7270	9.0650	9.3950	10.697	10.480	8.7380	9.6750	9.3700	9.1520	9.5390	9.3880
Na_2O	6.345	7.104	7.2880	5.9370	5.7270	4.9880	5.1660	6.0680	5.4480	5.920	6.1230	5.7630	5.8060
K_2O	0.238	0.313	0.3650	0.2470	0.2580	0.1540	0.1990	0.2790	0.2320	0.2210	0.2500	0.2110	0.2080
Total	98.5	99.3	99.9	99.5	98.8	99.1	99	99	98.8	99.6	100.3	99.3	99.6
Number of ions on basis of 32 oxygen													
Si	2.5509	2.6501	2.6637	2.5495	2.5251	2.4595	2.4688	2.5686	2.5081	2.5383	2.5503	2.5277	2.5398
Al	1.4597	1.3615	1.3504	1.4648	1.4880	1.5570	1.5448	1.4426	1.5103	1.4704	1.4590	1.4839	1.4700
Ca	0.4207	0.3392	0.3215	0.4374	0.4579	0.5211	0.5113	0.4242	0.4715	0.4527	0.4383	0.4608	0.4548
Na	0.5623	0.6186	0.6302	0.5184	0.5050	0.4397	0.4560	0.5331	0.4805	0.5175	0.5306	0.5037	0.5090
K	0.0139	0.0179	0.0208	0.0142	0.0150	0.0089	0.0116	0.0161	0.0135	0.0127	0.0143	0.0121	0.0120
An	42.20	34.76	33.06	45.09	46.82	53.74	52.23	43.58	48.84	46.05	44.58	47.18	46.61
Ab	56.40	63.40	64.81	53.44	51.65	45.34	46.59	54.76	49.77	52.65	53.97	51.58	52.16
Or	1.390	1.840	2.140	1.460	1.530	0.920	1.180	1.660	1.390	1.290	1.450	1.240	1.230

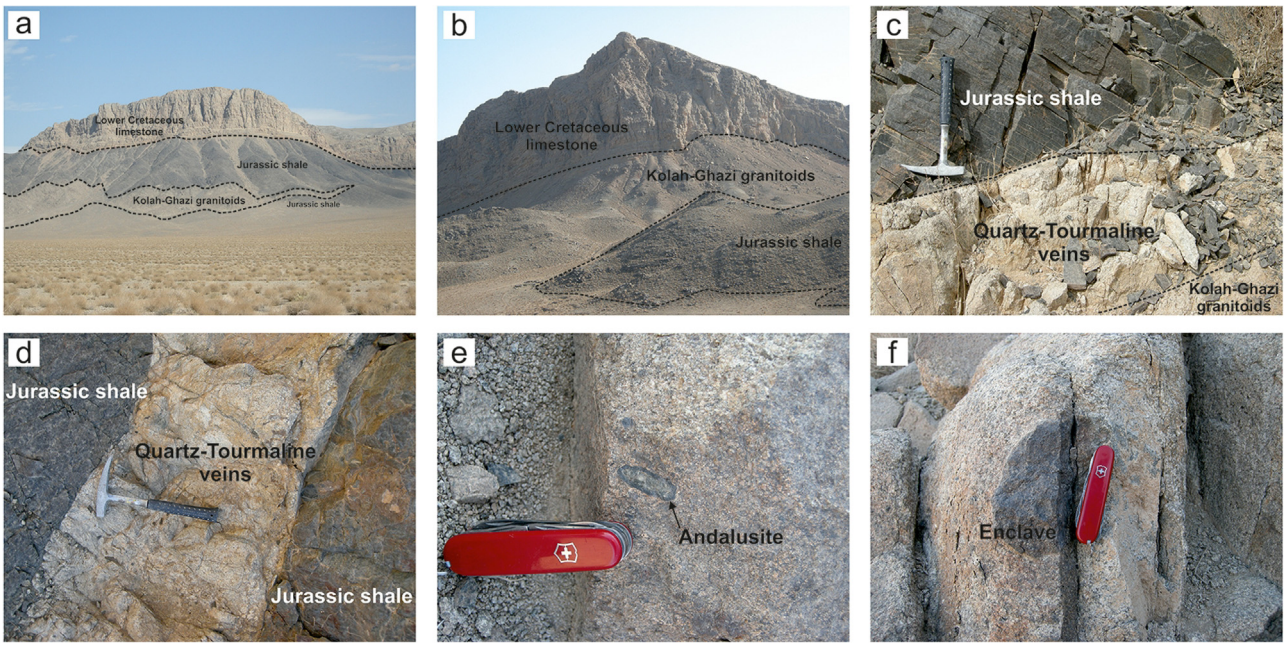

Fig. 3. Kolah-Ghazi granitoids: (A) and (B) Kolah-Ghazi granitoids intrude Jurassic shales and overlain by Cretaceous limestone; (C) boundary between Kolah-Ghazi granitoids and metamorphosed shales (slate); (D) Tourmaline-quartz vein in Kolah-Ghazi syenogranite; (E) Andalusite megacryst in granitoid; (F) Biotite-rich enclave in Kolah-Ghazi granitoid.

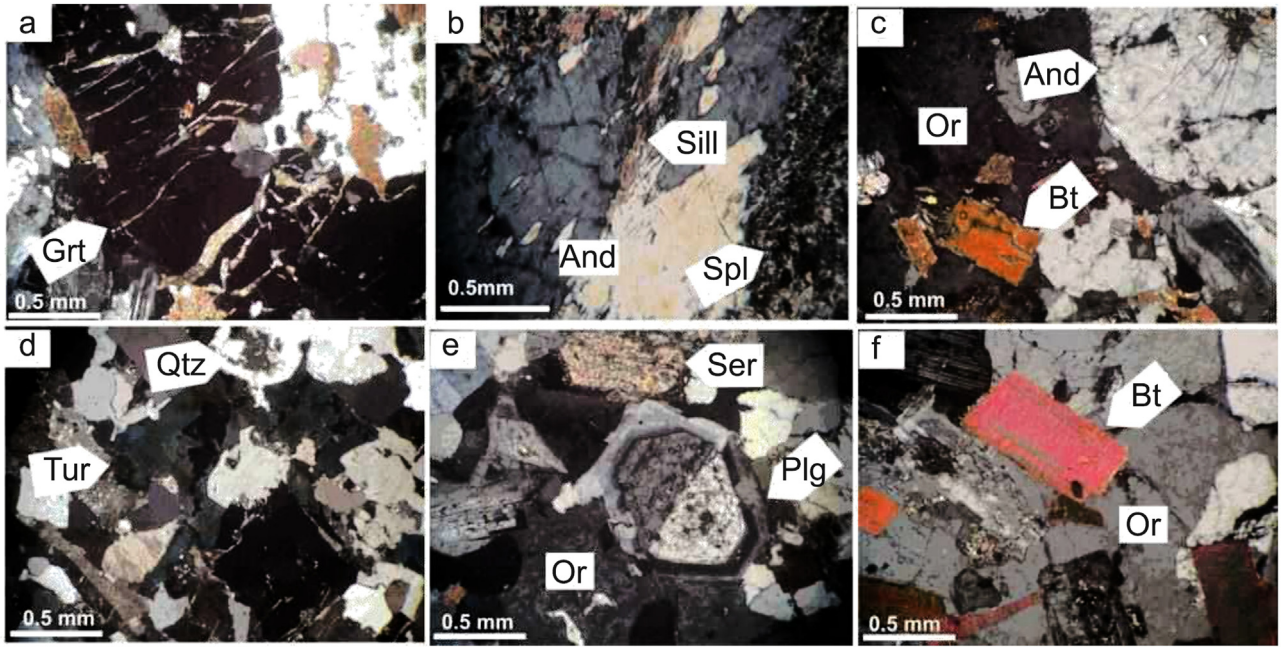

Fig. 4. Microphotographs of Kolah-Ghazi granitoid rocks: (A) fragmented garnet crystal in granodiorite; (B) Andalusite surrounded by a rim of spinel; (C) Andalusite, biotite and feldspar in granodiorite; (D) Tourmaline in syenogranite; (E) Zoning in plagioclase and replacement of plagioclase by sericite; (F) Biotite in monzogranite. Bt: biotite; Grt: garnet; Plg: plagioclase; Q: quartz; Tur: tourmaline; Or: orthoclase; And: andalusite; Ser: sericite.

the analyses were 20 kV, 20 nA, and 3 μm, respectively. Representative mineral compositions are reported in Tables 1–6 .

4.2. Whole rock analyses

Whole rock major element oxides were analyzed using a Rigaku RIX 2000 X-ray fluorescence spectrometer at Institute of Geology and Geophysics, Chinese Academy of Sciences (IGG-CAS) on fused glass beads. Concentrations of elements were determined by applying calibration curves established by regression data of 36 standard silicate samples encompassing a wide spectrum of compositions (Li et al., 2005). Precision for the analytical results is typically 2–5%. Trace elements were analyzed using an Agilent 7500a quadrupole ICP-MS at Guangzhou Institute of Geochemistry, Chinese Academy of Sciences (GIG-CAS) on a solution basis. About 50 mg of each powdered sample was dissolved in a high pressure Teflon bomb for 24 h using a $HF + HNO_3$ mixture. Analytical procedures are similar to those described by Li et al. (2000) . Counting signal drift was monitored by an internal standard Rh solution, whereas element concentrations of unknowns were calibrated using concurrently

Table 2
Selected electron microprobe analyses (EPMA) of cordierite from granitoid rocks.

No.	KM368B	KM-368B	KM-368B	KM-368B	KM-368B	KM-368B	KM-368B	KM-368B	KM-368B	KM368B
SiO_2	48.26	48.31	48.64	48.14	48.82	48.67	48.43	48.19	47.06	48.34
TiO_2	0.014	0.000	0.000	0.046	0.017	0.000	0.007	0.038	0.000	0.000
Al_2O_3	32.88	32.87	33.11	32.70	33.09	33.12	32.89	32.70	31.20	32.68
FeO	11.23	11.17	11.07	11.09	11.23	11.33	11.20	10.74	11.05	10.67
MnO	0.646	0.674	0.650	0.650	0.621	0.616	0.623	0.472	0.464	0.483
MgO	6.650	6.731	6.656	6.628	6.743	6.684	6.641	6.892	6.849	6.868
CaO	0.073	0.031	0.021	0.000	0.030	0.024	0.010	0.168	0.555	0.169
Na_2O	0.076	0.068	0.082	0.090	0.078	0.060	0.097	0.097	0.176	0.105
K2O	0.045	0.031	0.045	0.042	0.026	0.052	0.041	0.023	0.079	0.038
Total	99.92	99.92	100.4	99.47	100.7	100.6	100.0	99.39	97.54	99.49
Number of ions on basis of 18 oxygen										
Si	4.973	4.975	4.984	4.980	4.985	4.978	4.983	4.979	4.984	4.991
Ti	0.001	0.000	0.000	0.003	0.001	0.000	0.000	0.003	0.000	0.000
Al	3.992	3.989	3.998	3.988	3.983	3.993	3.988	3.982	3.895	3.977
Fe(ii)	0.968	0.962	0.948	0.959	0.959	0.965	0.963	0.928	0.979	0.921
Mg	1.022	1.033	1.016	1.022	1.027	1.019	1.019	1.062	1.081	1.057
Fe + Mg	1.989	1.995	1.965	1.981	1.985	1.989	1.982	1.990	2.060	1.979
Mg/Mg + Fe	0.513	0.518	0.517	0.516	0.517	0.512	0.514	0.533	0.525	0.534
Mn	0.056	0.059	0.056	0.057	0.054	0.053	0.054	0.041	0.042	0.042
Ca	0.008	0.003	0.002	0.000	0.003	0.003	0.001	0.018	0.063	0.019
Na	0.015	0.014	0.016	0.018	0.015	0.012	0.019	0.019	0.036	0.021
K	0.006	0.004	0.006	0.005	0.003	0.007	0.005	0.003	0.011	0.005
TOTAL	11.04	11.04	11.03	11.03	11.03	11.03	11.03	11.03	11.09	11.03

treated standards. Standards chosen include a set of USGS and Chinese national rock standards including BHVO-1, W- 2, AGV-1, G-2, GSR-1 and GSR-3, and analytical precision is typically better than 5%. Major and trace elements are presented in Table 7.

4.3. Zircon U-Pb dating

Zircon concentrates were separated from ca. 3 kg of rock samples using standard density and magnetic separation techniques. Zircon grains, together with zircon standards, were mounted in epoxy and then polished to section the crystals in half for analysis. Both optical photomicrographs and cathodoluminescence (CL) images were taken as a guide to isotopic analytical spot selection. The mount was vacuum-coated with high-purity gold prior to SIMS analyses.

Zircon U-Pb analyses were performed on a Cameca IMS-1280HR SIMS at the at the Institute of Geology and Geophysics, Chinese Academy of Sciences (IGG-CAS) in Beijing using standard operating conditions (7-scan duty cycle, ~8 nA primary O_2 beam, 20 × 30 μm analytical spot size, mass resolution ~5400). U-Th-Pb ratios and absolute abundances were determined relative to the standard zircon Plešovice (337 Ma, Sláma et al., 2008) and M257 (U = 840 ppm, Th/U = 0.27, Nasdala et al., 2008), respectively. Measured Pb isotopic compositions were corrected for common Pb using a ^{204}Pb-method. An average Pb of present-day crustal composition (Stacey and Kramers, 1975) is used for the common Pb assuming that it is largely due to surface contamination introduced during sample preparation. A long- term uncertainty of 1.5% (1 RSD) for ^{206}Pb/^{238}U measurements of the standard zircon was propagated to the unknowns (Li et al., 2010a). In order to monitor the external uncertainties of SIMS U-Pb measurements, analyses of an in-house zircon standard Qinghu were interspersed with unknowns. Ten analyses yield a weight mean ^{206}Pb/^{238}U age of 159.4 ± 1.8 Ma, identical within errors to the reported age of 159.5 ± 0.2 Ma (Li et al., 2013). Uncertainties on individual analyses in data table are reported at a 1σ level; mean ages for pooled U/Pb and Pb/Pb analyses are quoted with 95% confidence interval. Data reduction was carried out using an Isoplot/Ex v. 2.49 program (Ludwig, 2001). Zircon U-Th-Pb isotopic data are presented in Table 8.

5. Results

In the following section, we describe our analytical results, beginning with mineral compositions, then whole rock chemical compositions, then U-Pb zircon ages.

5.1. Mineral compositions

Compositions of feldspar, biotite, tourmaline, cordierite, andalusite, and sillimanite in the KGG rocks were analyzed by EPMA; representative analyses are listed in Tables 1–6, and characteristic features are described below.

5.1.1. Feldspars

Compositions of K-feldspar and plagioclase from syenogranite, monzogranite and granodiorite are given in Table 1. Plagioclase in syenogranite is more sodic than that from monzogranite and granodiorite. Syenogranite, granodiorite, and monzogranite show compositional variation from $An_{33.1}$ to $An_{46.8}$, $An_{44.6}$ to $An_{47.2}$, and $An_{43.6}$ to $An_{53.7}$, respectively. Rims and cores of individual grains have similar compositions.

5.1.2. Cordierite

Representative cordierite analyses from granodiorite are presented in Table 2. Cordierite is common in metapelite and anatectic migmatite (Clarke, 1995) and as an accessory mineral in S-type granitoid and rhyolite. Cordierite show a Mg/(Mg + Fe) ratio that varies between 0.51 and 0.53, with low Mn (0.04–0.05 a.p.f.u., based on 18 oxygens a.p.f.u.), and Na contents ranging from 0.01 to 0.03 a.p.f.u. Euhedral cordierites have Na_2O < 0.5 wt.% (up to 0.1 wt.%), suggesting they don't have a magmatic origin (Na_2O > 0.5 wt.%) (e.g., Bouloton, 1992; Villaseca and Barbero, 1994; Williamson et al., 1997). According to the nomenclature of Barbero and Villaseca (1992) and Pereira and Bea (1994), MnO versus CaO + K_2O + Na_2O and $\sum$chc (=Na + K) versus Mg/ (Mg + Fe + Mn) diagrams, respectively, which show different types of cordierite including metamorphic cordierite (I and M fields) magmatic cordierite (I and II fields) and fields for I and S type granites, cordierite from KGG the corresponds to metamorphic cordierite (Fig. 5a and b). KGG cordierite has similar Al^{IV} + Al^{VI}, Ca, Na, K and Mg as well as

Table 3
Selected electron microprobe analyses (EPMA) of biotite from granitoid rocks.

No.	KM-512	KM-512B	KM-389B	KM-389B	KM-389B	KM-389B	KM389B	KM-389B	KM-389B
SiO2	34.11	34.78	34.54	34.79	34.84	34.86	35.07	35.22	35.13
TiO2	3.034	3.185	4.033	3.854	3.958	3.600	3.814	4.276	3.808
Al2O3	17.00	17.31	16.85	16.69	16.76	16.79	16.57	16.80	16.82
FeO	27.66	27.39	24.55	24.51	24.61	24.36	23.50	24.70	24.33
MnO	0.190	0.181	0.204	0.209	0.213	0.196	0.252	0.260	0.221
MgO	6.045	5.821	7.371	7.356	7.344	7.546	7.704	7.309	7.550
CaO	0.068	0.000	0.021	0.034	0.000	0.018	0.000	0.027	0.000
Na2O	0.166	0.123	0.197	0.149	0.163	0.175	0.167	0.196	0.183
K2O	8.435	8.985	8.940	8.900	8.831	8.898	8.626	8.786	9.086
Total	99.1	98.9	100.3	100.1	99.6	99.4	99.2	100.2	89.9
Number of ions on basis of 11 oxygen									
Si	2.665	2.684	2.665	2.687	2.684	2.691	2.713	2.687	2.693
Al	1.335	1.316	1.334	1.312	1.316	1.309	1.286	1.313	1.307
Al	0.231	0.258	0.198	0.207	0.206	0.219	0.224	0.198	0.213
Ti	0.178	0.185	0.234	0.224	0.229	0.209	0.222	0.245	0.220
Fe^{3+}	0.194	0.205	0.211	0.222	0.229	0.213	0.253	0.246	0.215
Fe^{2+}	1.614	1.563	1.373	1.361	1.357	1.360	1.267	1.330	1.345
Fe TOTAL	1.808	1.768	1.584	1.583	1.586	1.573	1.520	1.576	1.560
Mg	0.704	0.669	0.848	0.847	0.843	0.868	0.888	0.831	0.863
Mg + Fe	2.512	2.437	2.432	2.430	2.429	2.442	2.408	2.407	2.423
Fe/Mg + Fe	0.719	0.725	0.651	0.651	0.653	0.644	0.631	0.650	0.644
Mg/Mg + Fe	0.280	0.275	0.349	0.348	0.347	0.356	0.369	0.345	0.356
Mn	0.012	0.012	0.013	0.014	0.014	0.013	0.016	0.017	0.014
Ca	0.006	0.000	0.002	0.003	0.000	0.001	0.000	0.002	0.000
Na	0.025	0.018	0.029	0.022	0.024	0.026	0.025	0.029	0.027
K	0.841	0.884	0.880	0.877	0.868	0.876	0.851	0.855	0.889
Total	7.806	7.795	7.789	7.778	7.771	7.787	7.747	7.754	7.785
OH•	2.000	2.000	2.000	2.000	2.000	2.000	2.000	2.000	2.000
MF	0.279	0.273	0.347	0.347	0.345	0.354	0.366	0.342	0.354
Al + Fe^{3+} + Ti	0.603	0.6481	0.643	0.654	0.664	0.641	0.699	0.689	0.647
Fe^{2+} + Mn	1.627	1.5749	1.386	1.375	1.371	1.373	1.284	1.34	1.359

No.	KM-389B	KM-432	KM-432	KM-432	KM-432	KM-432	KM-432	KM-432	KM-432
SiO2	35.47	34.67	34.68	34.94	35.37	35.64	35.54	35.88	35.57
TiO2	3.920	2.449	2.531	2.548	2.567	2.639	2.675	2.658	3.269
Al2O3	16.91	18.01	18.02	17.97	17.50	16.98	17.05	17.23	17.43
FeO	24.17	22.62	22.53	22.49	22.37	22.29	22.23	22.31	23.57
MnO	0.260	0.340	0.330	0.366	0.329	0.328	0.374	0.318	0.359
MgO	7.484	8.236	8.209	8.216	8.373	8.488	8.444	8.473	7.971
CaO	0.009	0.000	0.000	0.000	0.000	0.049	0.002	0.000	0.000
Na2O	0.147	0.131	0.119	0.166	0.178	0.171	0.175	0.192	0.162
K2O	8.900	9.029	8.815	8.909	8.844	8.650	8.665	8.655	8.947
Total	99.5	100.1	100	99.4	99.9	99.1	89.8	99.6	100.1
Number of ions on basis of 11 oxygen									
Si	2.707	2.682	2.684	2.693	2.710	2.735	2.736	2.746	2.699
Al	1.293	1.318	1.315	1.306	1.283	1.265	1.263	1.254	1.300
Al	0.227	0.322	0.328	0.326	0.302	0.271	0.283	0.299	0.258
Ti	0.225	0.143	0.147	0.147	0.148	0.152	0.155	0.153	0.187
Fe^{3+}	0.248	0.189	0.209	0.207	0.239	0.277	0.259	0.259	0.243
Fe^{2+}	1.294	1.274	1.249	1.243	1.198	1.153	1.172	1.168	1.254
Fe TOTAL	1.542	1.463	1.458	1.450	1.437	1.430	1.431	1.427	1.497
Mg	0.851	0.949	0.947	0.944	0.959	0.971	0.969	0.966	0.902
Mg + Fe	2.394	2.413	2.405	2.394	2.396	2.401	2.401	2.394	2.398
Fe/Mg + Fe	0.644	0.606	0.606	0.605	0.599	0.596	0.596	0.596	0.624
Mg/Mg + Fe	0.356	0.393	0.394	0.394	0.400	0.404	0.404	0.404	0.376
Mn	0.017	0.022	0.022	0.024	0.021	0.021	0.024	0.021	0.023
Ca	0.001	0.000	0.000	0.000	0.000	0.004	0.000	0.000	0.000
Na	0.022	0.019	0.018	0.025	0.026	0.025	0.026	0.028	0.023
K	0.866	0.891	0.870	0.876	0.867	0.847	0.851	0.845	0.866
Total	7.752	7.811	7.790	7.793	7.760	7.722	7.741	7.741	7.757
OH•	2.0000	2.000	2.000	2.000	2.000	2.000	2.000	2.000	2.000
MF	0.3532	0.389	0.390	0.390	0.396	0.401	0.399	0.400	0.372
Al + Fe^{3+} + Ti	0.7006	0.654	0.685	0.681	0.689	0.701	0.697	0.711	0.688
Fe^{2+} + Mn	1.3110	1.296	1.270	1.267	1.219	1.174	1.197	1.189	1.277

Mg/(Mg + Fe) values to metamorphic cordierite such as that from central Portugal (Pinto, 2001).

5.1.3. Biotite

Representative biotite analyses from monzogranite, granodiorite and syenogranite are presented in Table 3. The KGG biotites contain 5.8–8.5 wt.% MgO and 10.6–27.6 wt.% FeO (Table 3). Most are ferro-biotite (Fig. 6a) and show the chemical characteristics expected for primary (magmatic) biotites (Fig. 6b) and biotites of peraluminous igneous rocks (Fig. 6c). KGG biotites comprise considerable amounts of Al^{VI} (up to 1.4 a.p.f.u) and $Al^{IV} > 1.2$ a.p.f.u (Table 3), features ascribed to their coexistence with K- feldspar or other Al-rich minerals (garnet, andalusite and sillimanite) (Joyce, 1973). KGG biotites exhibit total Fe ranging from 1.4 to 1.8 a.p.f.u

Table 4
Selected electron microprobe analyses (EPMA) of tourmaline from granitoid rocks.

No.	Tur-Core	Tur-Core	Tur-Core	Tur-Core	Tur-Core	Tur-rim	Tur-rim	Tur-rim	Tur-rim
SiO_2	36.88	37.21	37.25	37.30	36.86	37.19	37.18	37.34	37.34
TiO_2	0.400	0.410	0.670	1.040	0.410	0.640	0.310	0.750	0.290
Al_2O_3	32.85	32.71	32.25	32.69	32.32	32.75	33.51	32.87	33.77
FeO	6.420	6.370	5.350	5.150	5.210	5.400	5.640	5.690	5.720
MnO	0.010	0.020	0.020	0.000	0.010	0.010	0.010	0.020	0.010
MgO	7.340	7.640	8.000	8.030	7.960	7.960	7.550	8.120	7.260
CaO	1.250	1.340	1.320	1.300	1.270	1.280	1.220	1.340	1.300
Na_2O	2.200	2.170	2.040	1.900	1.970	2.130	2.160	2.070	1.970
K2O	0.020	0.020	0.010	0.020	0.010	0.030	0.010	0.020	0.010
Total	87.6	88.5	86.9	88.8	87.6	90.4	88.8	87.9	91.9
Number of ions on basis of 31 O, OH, F									
Si	5.935	5.952	5.991	5.954	5.981	5.952	5.936	5.931	5.951
Ti	0.048	0.049	0.081	0.125	0.050	0.077	0.037	0.089	0.035
Al	6.230	6.167	6.113	6.150	6.180	6.177	6.305	6.153	6.342
Fe(ii)	0.864	0.852	0.719	0.687	0.707	0.723	0.753	0.756	0.762
Mg	1.761	1.822	1.918	1.911	1.926	1.899	1.797	1.923	1.725
Mg + Fe	2.624	2.674	2.638	2.598	2.633	2.622	2.550	2.678	2.487
Mg/Mg + Fe	0.671	0.681	0.727	0.735	0.731	0.724	0.705	0.718	0.693
Mn	0.001	0.003	0.003	0.000	0.001	0.001	0.001	0.002	0.001
Ca	0.215	0.230	0.227	0.222	0.221	0.219	0.209	0.228	0.222
Na	0.686	0.673	0.636	0.588	0.620	0.660	0.668	0.637	0.610
K	0.004	0.004	0.002	0.004	0.002	0.006	0.002	0.004	0.002
Na + K	0.690	0.678	0.638	0.592	0.621	0.667	0.670	0.641	0.610
TOTAL	15.75	15.75	15.69	15.64	15.69	15.71	15.71	15.72	15.65

Table 5
Selected electron microprobe analyses (EPMA) of andalusite and sillimanite from granitoid rocks.

	Granodiorite											
SiO2	36.70	36.85	37.01	36.87	36.77	36.97	37.15	36.91	36.65	37.04	36.73	36.98
TiO2	0.021	0.005	0.030	0.014	0.007	0.000	0.000	0.033	0.000	0.012	0.000	0.004
Al2O3	62.82	62.98	62.83	63.29	63.02	63.06	62.44	62.72	62.61	63.16	63.06	62.93
FeO	0.226	0.226	0.249	0.263	0.207	0.291	0.239	0.253	0.241	0.294	0.205	0.222
MnO	0.012	0.006	0.006	0.012	0.003	0.012	0.000	0.021	0.019	0.015	0.000	0.000
MgO	0.013	0.020	0.000	0.012	0.000	0.015	0.014	0.018	0.011	0.035	0.006	0.006
CaO	0.000	0.000	0.016	0.028	0.000	0.004	0.004	0.007	0.000	0.000	0.030	0.000
Na2O	0.022	0.014	0.012	0.058	0.041	0.049	0.000	0.005	0.024	0.029	0.038	0.033
K2O	0.000	0.011	0.005	0.018	0.003	0.034	0.007	0.011	0.017	0.026	0.016	0.009
Total	99.85	100.1	100.1	100	100.6	100.4	99.9	100	99.6	100.6	100.1	100.5
Number of ions on basis of 18 oxygen												
Si	0.596	0.596	0.598	0.595	0.596	0.597	0.603	0.598	0.597	0.597	0.595	0.598
Ti	0.000	0.000	0.000	0.000	8.530	0.000	0.000	0.000	0.000	0.000	0.000	4.870
Al	1.202	1.202	1.198	1.203	1.203	1.200	1.194	1.198	1.201	1.199	1.204	1.199
Fe(ii)	0.003	0.003	0.003	0.003	0.003	0.004	0.003	0.003	0.003	0.004	0.003	0.003
Mn	0.000	0.000	0.000	0.000	4.120	0.000	0.000	0.000	0.000	0.000	0.000	0.000
Mg	0.000	0.000	0.000	0.000	0.000	0.000	0.000	0.000	0.000	0.000	0.000	0.000
Ca	0.000	0.000	0.000	0.000	0.000	0.000	0.000	0.000	0.000	0.000	0.001	0.000
Na	0.001	0.000	0.000	0.001	0.001	0.001	0.000	0.000	0.001	0.001	0.001	0.001
K	0.000	0.000	0.000	0.000	0.000	0.001	0.000	0.000	0.000	0.001	0.000	0.000
TOTAL	1.803	1.803	1.802	1.805	1.803	1.804	1.800	1.802	1.803	1.804	1.804	1.802
SiO2	36.58	37.33	36.87	37.18	36.65	36.92	37.31	36.72	36.96	37.18	36.69	36.89
TiO2	0.042	0.038	0.000	0.035	0.023	0.000	0.005	0.051	0.000	0.003	0.017	0.000
Al2O3	63.14	62.85	63.20	62.75	63.19	62.89	63.09	63.22	62.86	62.77	62.93	62.72
FeO	0.263	0.222	0.221	0.185	0.252	0.244	0.245	0.232	0.191	0.231	0.187	0.180
MnO	0.000	0.006	0.006	0.025	0.000	0.000	0.020	0.001	0.000	0.000	0.000	0.000
MgO	0.019	0.001	0.003	0.017	0.006	0.000	0.012	0.017	0.003	0.008	0.007	0.000
CaO	0.007	0.003	0.025	0.013	0.000	0.025	0.000	0.023	0.021	0.013	0.000	0.000
Na2O	0.072	0.002	0.056	0.021	0.055	0.009	0.021	0.057	0.008	0.044	0.031	0.024
K2O	0.006	0.000	0.019	0.007	0.007	0.000	0.014	0.023	0.005	0.014	0.000	0.008
Total	100.4	100.3	100.2	100.1	100.7	100.3	100.1	100.3	100.1	100.2	99.9	99.8
Number of ions on basis of 13 oxygen												
Si	0.593	0.602	0.595	0.601	0.593	0.598	0.600	0.594	0.598	0.601	0.595	0.599
Ti	0.001	0.000	0.000	0.000	0.000	0.000	6.050	0.001	0.000	3.650	0.000	0.000
Al	1.205	1.194	1.203	1.195	1.205	1.200	1.196	1.204	1.199	1.196	1.204	1.199
Fe(ii)	0.003	0.003	0.003	0.002	0.003	0.003	0.003	0.003	0.002	0.003	0.002	0.002
Mn	0.000	8.200	8.210	0.000	0.000	0.000	0.000	1.370	0.000	0.000	0.000	0.000
Mg	0.000	2.400	7.220	0.000	0.000	0.000	0.000	0.000	7.240	0.000	0.000	0.000
Ca	0.000	0.000	0.000	0.000	0.000	0.000	0.000	0.000	0.000	0.000	0.000	0.000
Na	0.002	6.250	0.002	0.001	0.002	0.000	0.001	0.002	0.000	0.001	0.000	0.001
K	0.000	0.000	0.000	0.000	0.000	0.000	0.000	0.000	0.000	0.000	0.000	0.000
TOTAL	1.805	1.800	1.804	1.801	1.805	1.802	1.802	1.805	1.802	1.802	1.803	1.802

Table 6
Selected electron microprobe analyses (EPMA) of spinel from granitoid as well as volcanic rocks.

	Spl 1	Spl 2	Spl 3	Spl 4	Spl 5	Spl 6	Spl 7	Spl 8
SiO2	0.010	0.030	0.020	0.030	0.040	0.020	0.030	0.030
TiO2	0.020	0.010	0.060	0.030	0.040	0.020	0.050	0.030
Al2O3	60.47	60.36	60.00	60.21	60.04	60.42	60.11	60.26
FeO	34.45	34.50	34.54	34.69	34.64	34.48	34.62	34.55
MnO	0.480	0.490	0.500	0.480	0.420	0.490	0.490	0.450
MgO	4.380	4.320	4.037	4.280	4.220	4.350	4.320	4.300
ZnO	0.510	0.520	0.470	0.590	0.510	0.520	0.530	0.510
Total	100.3	100.2	99.96	100.3	99.91	100.2	100.1	100.1
Number of ions on basis of 32 oxygen								
Si	0.002	0.007	0.005	0.007	0.009	0.004	0.007	0.007
Ti	0.003	0.002	0.010	0.005	0.007	0.003	0.008	0.005
Al	15.94	15.93	15.95	15.90	15.92	15.94	15.90	15.93
Cr	0.000	0.000	0.000	0.000	0.000	0.000	0.000	0.000
Fe(ii)	6.440	6.460	6.510	6.510	6.510	6.450	6.490	6.480
Mn	0.090	0.090	0.090	0.090	0.080	0.080	0.090	0.090
Mg	1.460	1.440	1.360	1.430	1.410	1.450	1.440	1.440
Zn	0.080	0.080	0.080	0.090	0.080	0.080	0.080	0.090

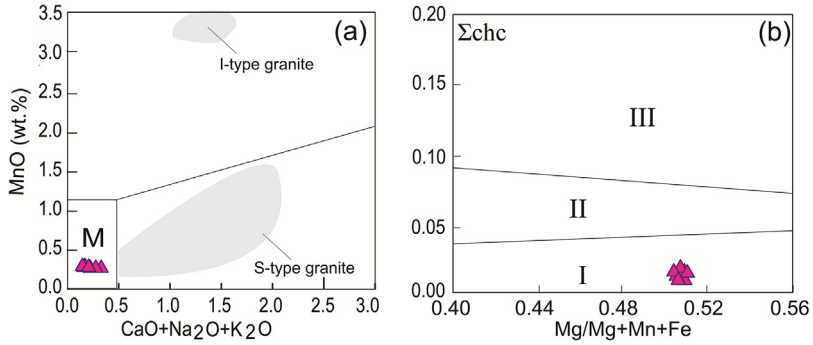

Fig. 5. (a) Composition of cordierite in the discriminant diagram MnO vs. ($Na_2O + K_2O + CaO$) Compositional fields for metamorphic (M field) and igneous (S- and I-type granites) cordierite come from data of Barbero and Villaseca (1992) and Villaseca and Barbero (1994). (b) Binary plot of Σchc (= Na + K) vs. Mg/(Fe + Mg + Mn) for cordierite (Pereira and Bea, 1994). I: metamorphic cordierite; II and III magmatic cordierite with different zoning.

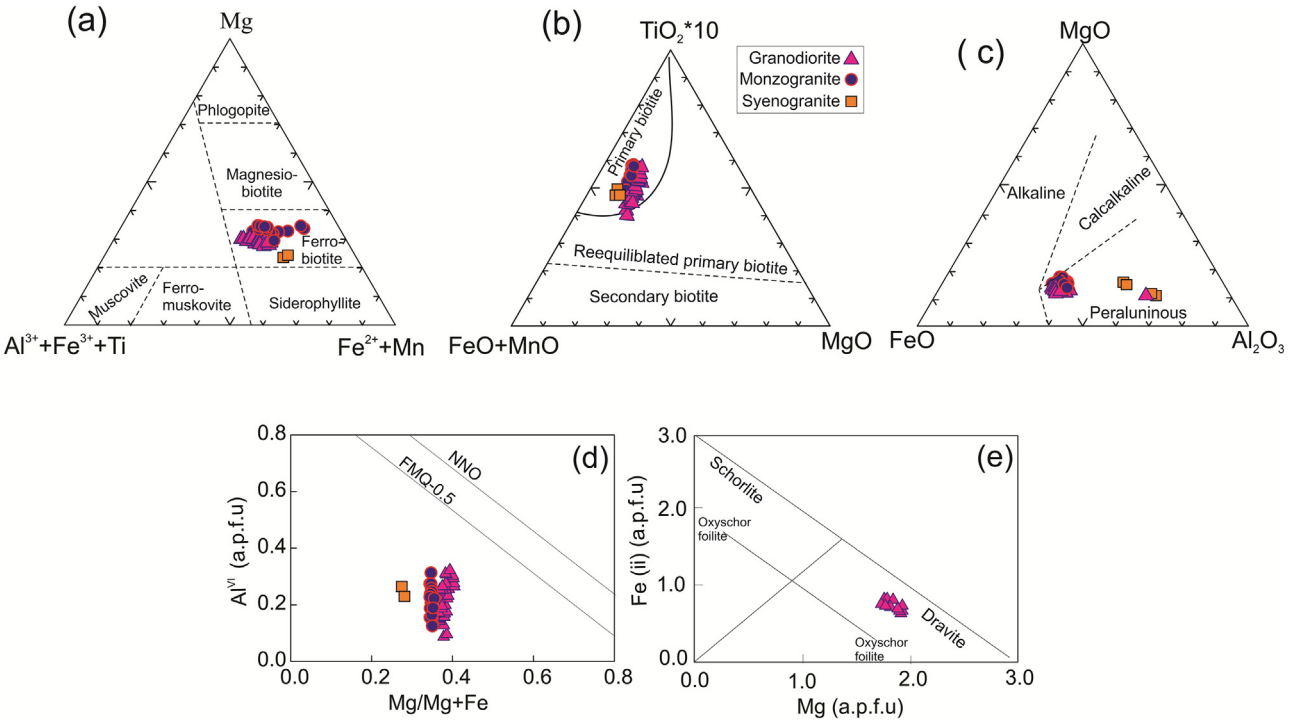

Fig. 6. Compositional plots of biotites. (a) KGG biotites mainly plot in the ferro-biotite field of Mg–($Al^{VI} + Fe^{3+}$ + Ti)– (Fe^{2+} + Mn) ternary diagram (Foster, 1960), (b) in the primary biotite field of the $10*TiO_2$– FeO_{total}–MgO diagram (Nachit et al., 2005), and (c) in the field of peraluminous magma on the MgO–FeO^*–Al_2O_3 diagram (Abdel-Rahman, 1994), (d) and (e) Binary plots of AlVI vs. Mg/Mg + Fe and Fe vs. Mg for tourmalines from KGG. NNO, nickel-nickel oxide; FMQ, fayalite-magnetite- quartz.

Table 7
Major and trace element contents of the KGG.

sample	YL-KG-351 Monzogranite	YL-KG-366B Monzogranite	YL-KG-389A Monzogranite	YL-KG-413 Monzogranite	YL-KG-396 Monzogranite	YL-KG-443 Monzogranite	YL-KG-432 Monzogranite	YL-KG-460 Monzogranite	YL-KG-486 Monzogranite
SiO2	69.5	62.4	54.9	68.3	69.7	65.9	65.4	67.9	67.1
TiO2	0.38	0.81	0.73	0.44	0.32	0.54	0.63	0.46	0.54
Al2O3	15	15.7	16.9	15.8	15.4	16.5	15.1	14.8	15.3
MnO	0.09	0.08	0.26	0.11	0.06	0.11	0.11	0.06	0.09
FeO	4.18	7.51	11.39	4.59	3.39	5.08	5.73	4.21	5.19
MgO	1.02	2.96	5.05	1.23	0.91	1.73	1.86	1.36	1.63
CaO	2.35	3.36	5.12	2.49	2.46	2.36	3.02	2.18	2.69
Na2O	2.34	2.38	1.33	2.42	2.62	2.44	2.24	2.25	2.23
K2O	3.77	2.56	2.21	3.76	3.85	4.09	3.25	4.34	3.41
P2O5	0.16	0.14	0.1	0.16	0.15	0.14	0.14	0.13	0.13
LOI	1.26	2.16	1.42	1.24	1.18	1.66	1.42	1.32	1.32
Total	100	100	99.4	100.5	100	100.5	99	99	99.6
Li	98.90	134.5	93.70	96.7	115.35	112.0	114.8	102.4	129.0
Sc	10.08	23.1	38.77	9.59	8.44	14.62	18.15	12.75	15.65
V	35.29	131.45	206.5	43.5	27.21	64.14	81.22	59.60	67.69
Cr	26.39	100.75	233.2	32.0	20.73	49.50	60.13	43.59	49.14
Co	6.75	19.78	24.91	8.41	5.41	11.15	13.29	9.01	11.15
Ni	13.99	27.85	31.58	15.41	11.67	18.33	20.71	16.37	19.08
Cu	13.79	30.28	75.35	28.63	8.04	17.63	26.06	8.52	22.79
Zn	57.72	69.43	177.23	145.9	52.44	79.11	76.92	63.24	73.28
Ga	17.75	18.34	18.42	18.00	18.07	18.34	18.47	16.38	17.62
Rb	166.61	154.34	148.27	173.92	168.82	185.13	154.58	185.29	156.80
Sr	112.66	149.35	128.87	121.59	124.25	156.32	124.99	99.67	114.90
Y	32.77	29.06	19.69	30.99	31.98	30.31	29.16	28.71	33.81
Zr	143.31	141.98	78.35	145.68	134.56	144.45	184.05	128.31	133.96
Nb	11.62	10.66	8.55	12.16	10.79	11.97	12.80	10.65	11.21
Cs	11.29	7.37	14.13	12.98	11.50	10.59	9.40	14.19	12.02
Ba	372.47	294.02	244.65	365.62	432.06	416.91	339.01	524.65	317.01
La	37.63	25.45	13.41	37.45	36.16	32.61	31.19	28.14	27.50
Ce	76.00	52.88	27.52	76.19	73.47	67.96	64.39	58.55	56.94
Pr	8.75	6.08	3.16	8.76	8.46	7.70	7.33	6.79	6.51
Nd	33.09	23.44	12.40	33.30	32.19	29.41	28.04	25.97	24.90
Sm	6.88	5.16	2.98	6.86	6.73	6.26	5.93	5.67	5.46
Eu	1.00	1.10	0.94	1.03	1.08	1.04	1.01	0.93	0.94
Gd	6.04	4.85	3.06	6.06	6.02	5.60	5.37	5.19	5.13
Tb	0.95	0.80	0.54	0.94	0.96	0.89	0.85	0.85	0.87
Dy	5.68	4.88	3.36	5.51	5.60	5.32	5.07	4.97	5.52
Ho	1.16	1.02	0.71	1.10	1.13	1.07	1.03	1.00	1.21
Er	3.20	2.86	2.08	2.93	2.97	2.89	2.80	2.69	3.40
Tm	0.48	0.44	0.35	0.43	0.44	0.44	0.43	0.41	0.54
Yb	3.06	2.84	2.38	2.67	2.77	2.78	2.75	2.55	3.46
Lu	0.46	0.43	0.37	0.40	0.41	0.42	0.42	0.38	0.52
Hf	3.99	3.87	2.19	4.16	3.94	3.94	5.03	3.69	3.80
Ta	0.81	0.73	0.55	0.79	0.83	0.80	0.81	0.76	0.76
Pb	26.74	15.52	17.82	33.43	27.89	29.78	22.64	30.40	22.60
Th	14.52	9.33	4.30	14.98	14.59	12.66	11.86	12.77	11.03
U	1.49	1.85	2.13	1.56	1.98	1.65	1.69	1.59	1.58

sample	YL-KG-538 Monzogranite	YL-KG-547A Monzogranite	YL-KG-547B Monzogranite	YL-KG-512A Granodiorite	YL-KG-518 Syenogranite	YL-KG-553 Syenogranite	YL-KG-476 Granodiorite
SiO2	67.5	68.8	69.2	53.4	68.6	71.7	64.2
TiO2	0.51	0.28	0.31	1.02	0.39	0.21	0.69
Al2O3	14.9	14.3	15.3	17.9	14.9	14.6	16.3
MnO	0.05	0.08	0.07	0.2	0.07	0.04	0.09
FeO	5.35	4.21	4.26	12.3	4.11	3.02	6.03
MgO	1.51	0.74	0.83	2.88	1.24	0.51	2.07
CaO	2.08	1.21	1.13	1.21	1.59	1.16	3.19
Na2O	2.56	2.53	2.75	2.31	2.31	2.93	2.48
K2O	4.10	4.75	4.31	4.19	4.47	4.75	3.16
P2O5	0.15	0.17	0.17	0.11	0.15	0.16	0.15
LOI	1.58	1.52	1.74	3.16	1.88	1.22	1.56
Total	100.3	98.6	100	98.7	99.7	100.3	99.9
Li	126.3	100.1	105.	223	91.5	64.3	111
Sc	14.09	9.42	9.51	33.3	9.56	5.01	18.5
V	60.73	27.6	30.3	124	43.4	15.6	86.2
Cr	38.38	22.3	24.0	134	33.8	12.7	60.9
Co	10.56	5.29	6.16	25.7	7.65	4.07	12.3
Ni	17.16	10.1	11.9	54.8	14.9	8.19	20.9
Cu	26.38	28.6	25.4	217.	28.8	14.7	38.7
Zn	169.9	204.	232.	210.	115	86.3	97.8
Ga	18.23	18.8	20.1	31.6	17.7	17.7	19.9
Rb	271.8	2146	203.	344	190	136	162
Sr	154.9	147.5	159.	85.6	154.	120	138
Y	22.93	19.95	19.6	30.7	28.6	12.2	29.8

Table 7 (*Continued*)

sample	YL-KG-538 Monzogranite	YL-KG-547A Monzogranite	YL-KG-547B Monzogranite	YL-KG-512A Granodiorite	YL-KG-518 Syenogranite	YL-KG-553 Syenogranite	YL-KG-476 Granodiorite
Zr	122.3	130.3	139	194	132	136	165
Nb	11.88	13.31	13.4	35.9	13.0	12.6	13.5
Cs	19.44	10.36	9.95	23.4	10.5	5.87	13.3
Ba	303.5	553.2	433	372	443	435	329
La	26.06	24.67	28.4	30.7	28.2	15.8	34.6
Ce	54.13	51.32	60.3	63.5	57.7	34.3	72.6
Pr	6.180	6.05	6.92	7.29	6.67	4.43	8.23
Nd	23.53	23.4	26.7	27.5	25.3	17.8	31.5
Sm	5.14	5.36	5.94	5.95	5.52	4.35	6.66
Eu	0.93	1.19	1.24	0.71	0.99	0.99	1.08
Gd	4.55	4.52	4.89	5.40	5.07	3.62	5.88
Tb	0.71	0.66	0.69	0.87	0.83	0.49	0.91
Dy	4.11	3.61	3.67	5.19	4.87	2.63	5.40
Ho	0.79	0.72	0.70	1.05	1.00	0.50	1.06
Er	2.14	1.94	1.88	2.84	2.67	1.33	2.87
Tm	0.33	0.30	0.28	0.42	0.39	0.20	0.43
Yb	2.08	1.98	1.86	2.66	2.28	1.30	2.75
Lu	0.31	0.30	0.28	0.40	0.33	0.20	0.41
Hf	3.58	3.96	4.20	5.92	3.78	4.01	4.50
Ta	0.95	1.06	1.16	2.43	0.93	0.89	0.92
Pb	21.05	39.43	33.22	24.90	33.81	35.35	18.86
Th	11.08	10.08	10.50	12.72	11.94	8.43	12.78
U	1.910	1.73	1.70	2.21	1.90	1.27	1.57

and Fe/(Fe + Mg) from 0.5 to 0.7 in contrast to the values found in I- type granites (0.5–1.2 a.p.f.u and 0.3–0.9 for Fe and Fe/Fe + Mg, respectively) (Pesquera et al., 2013).

5.1.4. Tourmaline

Tourmaline is common and occurs as an accessory mineral coexisting with biotite, cordierite and andalusite. Tourmalines belong mostly to the alkali group, according to the nomenclature of Henry et al. (2011), with (Na + K) > 0.50 a.p.f.u. (Table 4). Most tourmaline compositions fall into the dravitic field, with Mg/(Mg + Fe) ratios in the range of 0.67–0.73 (Fig. 6d and e).

5.1.5. Andalusite and sillimanite

Andalusite and sillimanite occur as accessory minerals in peraluminous granodiorite, syenogranite and monzogranite (Table 5). Since andalusite and sillimanite of syenogranite and monzogranite are altered, representative analyses are only from granodiorite, listed in Table 5. They are relatively pure, containing up to 0.3 wt.% FeO. They contain up to 0.003 a.p.f.u. Fe and undetectable Mg impurities.

5.1.6. Spinel

Spinel exists as accessory minerals in granodiorite in association with andalusite. All analyzed spinels are rich in Fe and Al, contain low Zn (0.08–0.09 a.p.f.u), barely detectable Ti (up to 0.01 a.p.f.u), and no Cr. Calculated Fe^{+3} contents are <0.12 a.p.f.u. Mg contents range from 1.3 to 1.4 a.p.f.u. (Table 6). This spinel is hercynite, commonly found in high grade metasediments.

5.2. Whole rock chemistry

Representative whole rock analyses of the KGG are presented in Table 7. The KGG samples show a wide range of silica (53.4-71.7 wt.%), Al_2O_3 (14.3- 17.9 wt.%) and K_2O (2.21–4.75 wt.%) contents. In the normative QAP diagram (Fig. 7a) after (Streckeisen, 1973), the KGG rocks plot predominantly in the field of monzogranites, granodiorites and alkali feldspar syenites. The mostly high alumina saturation index (ASI) (1.65–2.32; averaging 1.82) and the appearance of normative corundum (1.65–2.32 wt%) indicate a peraluminous character for the KGG. In the K_2O versus Na_2O diagram (Chapell and White, 1983) and A/CNK versus A/NK diagram (Shand, 1943), KGG samples plot in the field of peraluminous S- type granites (Fig. 7b) similar to S-type granites of the Lachlan fold belt (Fig. 7c). In the Harker diagrams, most elements exhibit slight linear trends, except for K_2O (Fig. 8). For these granitoid rocks, Fe_2O_3, MgO, TiO_2, Al_2O_3, Zr, Rb, Sr concentrations decrease and K_2O and Ba concentrations increase with increasing SiO_2 (Figs. 8 and 9).

In the N-MORB normalized variation diagram, the KGG shows LREE and LILE enriched pattern ($La/Yb_n \approx 8.29$) and depletion in HFSE, Ba, Ti, P, Nb, Sr and Enrichment in Th, U, K and Nd elements (Fig. 9a). Chondrite-normalized REE patterns are characterized by light rare-earth elements (LREEs) relative to heavy rare earth elements (HREEs) (Fig. 9b). They are depleted in HFSE, Th, Nb, Ta, Ti, P, Ba and Sr and enriched in Rb, U, Th, K, and Nd relative to LREEs (Fig. 9a and b). In the Rb against Y + Nb diagram (Pearce et al., 1984), the KGG rocks show affinities to volcanic arc granites (VAG) (Fig. 10a). In the Nb/16 - Rb/100 - Y/44 tectonic diagram proposed by Thieblemont and Cabanis (1990), the KGG samples plot in the *syn*-subduction and post collision field (Fig. 10b and c).

5.3. U–Pb zircon geochronology

Zircons from monzogranite (1 sample), granodiorite (2 samples), syenogranite (1 sample) were dated using SIMS method. Analytical results for U–Pb zircon geochronology are given in Table 8 and shown on $^{207}Pb/^{206}Pb$ versus $^{238}U/^{206}Pb$ Concordia diagrams (Tera and Wasserburg, 1972), where the analytical points locate along a mixing line between the common Pb composition in the upper intercept and the crystallization age in the lower intercept (Fig. 12). This method is commonly used to date young zircons (Claoué-Long et al., 1995).

5.3.1. Monzogranite (YL-KG-374)

Zircons from the monzogranite are colorless, euhedral to subhedral prismatic, and characterized by regular concentric zoning in cathodoluminescence (CL) images (Fig. 11a). They range in length from 100 to 200 μm, with length to width ratios between 1:1 and 2:1. These zircons contain U (151–1028 ppm) and Th (66–741 ppm) contents and Th/U ratios of 0.07–0.34. Fifteen analyzed grains show the intercept age of 169.3 ± 1.9 Ma (MSWD = 1.7) (Fig. 12a).

Table 8
U–Pb zircon data of the KGG samples.

sample/ spot #	$^{207}Pb/^{235}U$	±σ %	$^{206}Pb/^{238}U$	±σ %	$^{238}U/^{206}Pb$	±σ %	$^{207}Pb/^{206}Pb$	±σ %	$^{238}U/^{206}Pb$	±σ %	$^{207}Pb/^{206}Pb$	±σ %	$^{207}Pb/^{206}Pb$	±σ	$^{207}Pb/^{235}U$	±σ	$^{206}Pb/^{238}U$	±σ	207-corr age (Ma)	±σ	[U] ppm	[Th] ppm	[Pb] ppm	Th/U meas	f_{206}%
YL-KG-491	0.16939	1.87	0.0256	1.54	39.121	1.54	0.04806	1.07	39.121	1.54	0.04806	1.07	102.3	25.0	158.9	2.8	162.7	2.5	163.0	2.5	483	95	14	0.092	{0.16}
YL-KG-491	0.17786	2.99	0.0256	1.68	39.014	1.68	0.05033	2.48	38.905	1.68	0.05251	1.84	210.1	56.4	166.2	4.6	163.2	2.7	162.9	2.7	213	36	6	0.078	{0.28}
YL-KG-491	0.17493	2.06	0.0258	1.59	38.716	1.59	0.04912	1.32	38.716	1.59	0.04912	1.32	153.5	30.6	163.7	3.1	164.4	2.6	164.4	2.6	332	201	11	0.284	{0.16}
YL-KG-491	0.17793	2.09	0.0262	1.51	38.236	1.51	0.04934	1.45	38.236	1.51	0.04934	1.45	164.1	33.5	166.3	3.2	166.4	2.5	166.4	2.5	408	273	14	0.314	{0.15}
YL-KG-491	0.17703	3.54	0.0262	2.29	38.175	2.29	0.04901	2.70	38.050	2.29	0.05160	2.15	148.5	62.1	165.5	5.4	166.7	3.8	166.8	3.8	285	69	8	0.114	{0.33}
YL-KG-491	0.18295	2.01	0.0265	1.50	37.678	1.50	0.04999	1.34	37.678	1.50	0.04999	1.34	194.7	30.9	170.6	3.2	168.9	2.5	168.7	2.5	349	115	11	0.154	{0.29}
YL-KG-491	0.18147	2.16	0.0267	1.52	37.465	1.52	0.04931	1.54	37.398	1.52	0.05072	1.24	162.5	35.7	169.3	3.4	169.8	2.5	169.8	2.6	397	64	12	0.076	{0.18}
YL-KG-491	0.17808	2.51	0.0269	1.58	37.188	1.58	0.04803	1.95	37.188	1.58	0.04803	1.95	100.8	45.5	166.4	3.9	171.1	2.7	171.4	2.7	146	54	5	0.173	{0.40}
YL-KG-491	0.18360	2.30	0.0269	1.54	37.146	1.54	0.04946	1.71	37.108	1.54	0.05027	1.55	169.8	39.4	171.2	3.6	171.2	2.6	171.3	2.6	286	51	9	0.084	{0.10}
YL-KG-491	0.18673	2.33	0.0270	1.86	37.066	1.86	0.05020	1.41	37.066	1.86	0.05020	1.41	204.1	32.3	173.8	3.7	171.6	3.1	171.5	3.2	308	175	10	0.267	>1e6
YL-KG-491	0.18271	2.24	0.0273	1.53	36.598	1.53	0.04850	1.64	36.526	1.53	0.05003	1.33	123.6	38.1	170.4	3.5	173.8	2.6	174.0	2.6	450	79	14	0.083	{0.20}
YL-KG-491	0.18591	2.34	0.0274	1.70	36.469	1.70	0.04917	1.61	36.420	1.70	0.05024	1.43	156.1	37.2	173.1	3.7	174.4	2.9	174.5	2.9	509	216	16	0.199	{0.14}
YL-KG-491	0.18540	2.07	0.0275	1.51	36.407	1.51	0.04896	1.42	36.346	1.51	0.05027	1.26	145.7	33.0	172.7	3.3	174.7	2.6	174.8	2.6	884	701	32	0.372	{0.17}
YL-KG-491	0.18927	1.89	0.0275	1.50	36.402	1.50	0.04997	1.14	36.391	1.50	0.50200	1.12	193.6	26.3	176.0	3.1	174.7	2.6	174.6	2.6	474	71	14	0.071	{0.03}
YL-KG-491	0.18352	2.60	0.0275	1.64	36.336	1.64	0.04836	2.02	36.336	1.64	0.04836	2.02	117.1	46.9	171.1	4.1	175.0	2.8	175.3	2.9	154	57	5	0.173	{0.72}
YL-KG-491	0.18915	2.44	0.0278	1.52	36.027	1.52	0.04942	1.91	35.941	1.52	0.05129	1.51	167.9	44.0	175.9	3.9	176.5	2.6	176.5	2.7	359	51	11	0.066	{0.24}
YL-KG-491	0.18715	2.17	0.0281	1.50	35.619	1.50	0.04835	1.57	35.619	1.50	0.04835	1.57	116.3	36.6	174.2	3.5	178.5	2.6	178.8	2.7	488	145	16	0.139	{0.14}
YL-KG-374	0.17228	2.36	0.0262	1.53	38.173	1.53	0.04770	1.80	38.047	1.53	0.05030	1.13	84.3	42.3	161.4	3.5	166.7	2.5	167.1	2.5	420	157	13	0.169	{0.33}
YL-KG-374	0.17430	3.01	0.0263	1.50	38.093	1.50	0.04816	2.60	37.859	1.51	0.05300	1.13	106.9	60.4	163.1	4.5	167.0	2.5	167.3	2.5	375	148	11	0.179	{0.62}
YL-KG-374	0.17416	3.87	0.0263	1.57	37.970	1.57	0.04796	3.54	37.685	1.56	0.05388	1.85	97.3	81.7	163.0	5.8	167.6	2.6	167.9	2.6	151	66	5	0.198	{0.75}
YL-KG-374	0.17282	3.57	0.0263	1.66	37.974	1.66	0.04760	3.16	37.732	1.66	0.05261	1.90	79.3	73.4	161.9	5.4	167.6	2.8	167.9	2.8	334	119	10	0.162	{0.64}
YL-KG-374	0.17635	2.63	0.0265	1.56	37.774	1.56	0.04831	2.11	37.601	1.56	0.05193	1.31	114.6	49.1	164.9	4.0	168.4	2.6	168.7	2.6	282	111	9	0.178	{0.46}
YL-KG-374	0.17474	2.37	0.0265	1.53	37.719	1.53	0.04780	1.82	37.546	1.53	0.05142	1.03	89.5	42.5	163.5	3.6	168.7	2.5	169.0	2.6	492	192	15	0.177	{0.46}
YL-KG-374	0.18337	1.85	0.0269	1.50	37.243	1.50	0.04953	1.08	37.243	1.50	0.04953	1.08	173.0	25.1	171.0	2.9	170.8	2.5	170.8	2.5	432	154	13	0.161	{0.35}
YL-KG-374	0.18471	1.90	0.0270	1.50	37.031	1.50	0.04961	1.17	36.977	1.50	0.05076	1.02	176.6	27.1	172.1	3.0	171.8	2.5	171.7	2.6	731	551	25	0.341	{0.15}
YL-KG-374	0.17950	2.42	0.0270	1.51	37.058	1.51	0.04825	1.89	36.919	1.51	0.05120	1.30	111.3	43.9	167.6	3.7	171.6	2.6	171.9	2.6	358	114	11	0.145	{0.38}
YL-KG-374	0.18552	1.81	0.0271	1.52	36.944	1.52	0.04971	0.98	36.944	1.52	0.04971	0.98	181.4	22.7	172.8	2.9	172.2	2.6	172.1	2.6	601	104	18	0.079	{0.15}
YL-KG-374	0.18138	2.90	0.0272	1.51	36.762	1.51	0.04836	2.47	36.535	1.51	0.05322	1.65	116.9	57.3	169.2	4.5	173.0	2.6	173.3	2.6	369	219	12	0.269	{0.62}
YL-KG-374	0.17744	3.01	0.0276	1.57	36.257	1.57	0.04666	2.57	35.898	1.56	0.05447	1.32	31.8	60.5	165.9	4.6	175.4	2.7	176.0	2.7	443	128	14	0.131	{0.99}
YL-KG-374	0.18953	1.93	0.0282	1.53	35.433	1.53	0.04871	1.18	35.318	1.53	0.05126	0.71	133.7	27.5	176.2	3.1	179.4	2.7	179.6	2.7	973	741	35	0.345	{0.32}
YL-KG-374	0.19055	2.90	0.0285	1.61	35.074	1.61	0.04847	2.42	34.884	1.61	0.05273	2.04	122.3	56.0	177.1	4.7	181.2	2.9	181.5	2.9	1190	159	37	0.061	{0.54}
YL-KG-513	0.16882	2.66	0.0257	1.54	38.931	1.54	0.04767	2.17	38.728	1.54	0.05177	1.28	82.7	50.8	158.4	3.9	163.5	2.5	163.8	2.5	301	40	8	0.061	{0.52}
YL-KG-513	0.17242	3.75	0.0259	2.17	38.642	2.17	0.04832	3.05	38.480	2.17	0.05162	2.44	115.1	70.4	161.5	5.6	164.7	3.5	164.9	3.6	273	53	8	0.087	{0.42}
YL-KG-513	0.17998	2.68	0.0262	1.50	38.177	1.50	0.04984	2.22	37.955	1.50	0.05441	1.27	187.3	50.8	168.0	4.2	166.7	2.5	166.6	2.5	535	96	15	0.082	{0.58}
YL-KG-513	0.17164	3.41	0.0262	1.67	38.221	1.67	0.04758	2.97	37.980	1.67	0.05256	1.43	78.4	69.1	160.8	5.1	166.5	2.7	166.9	2.8	260	86	8	0.150	{0.63}
YL-KG-513	0.18402	1.92	0.0264	1.62	37.921	1.62	0.05061	1.03	37.921	1.62	0.05061	1.03	223.1	23.7	171.5	3.0	167.8	2.7	167.5	2.7	655	46	19	0.032	{0.39}
YL-KG-513	0.18356	1.96	0.0265	1.55	37.795	1.55	0.05032	1.20	37.795	1.55	0.05032	1.20	209.6	27.6	171.1	3.1	168.3	2.6	168.2	2.6	331	94	10	0.128	{0.30}
YL-KG-513	0.18922	2.32	0.0267	1.65	37.500	1.65	0.05146	1.63	37.500	1.65	0.05146	1.63	261.7	37.1	176.0	3.8	169.7	2.8	169.2	2.8	325	170	10	0.237	{0.54}
YL-KG-513	0.18377	2.38	0.0266	1.73	37.527	1.73	0.05002	1.64	37.527	1.73	0.05002	1.64	195.8	37.7	171.3	3.8	169.5	2.9	169.4	2.9	257	51	8	0.090	{0.23}
YL-KG-513	0.17588	2.25	0.0266	1.51	37.612	1.51	0.04798	1.66	37.428	1.51	0.05183	1.11	98.2	38.9	164.5	3.4	169.2	2.5	169.5	2.5	649	172	19	0.120	{0.49}
YL-KG-513	0.17996	2.33	0.0267	1.52	37.474	1.52	0.04891	1.77	37.381	1.51	0.05085	1.36	143.5	41.0	168.0	3.6	169.8	2.5	169.9	2.6	278	88	8	0.144	{0.25}
YL-KG-513	0.17242	5.24	0.0266	1.68	37.557	1.68	0.04696	4.96	37.174	1.67	0.05500	2.96	47.4	114.5	161.5	7.9	169.4	2.8	169.9	2.8	869	81	25	0.042	{1.02}
YL-KG-513	0.18619	2.44	0.0268	1.50	37.372	1.50	0.05047	1.92	37.372	1.50	0.05047	1.92	216.6	43.8	173.4	3.9	170.2	2.5	170.0	2.5	263	106	8	0.182	{0.64}
YL-KG-513	0.19157	1.82	0.0269	1.50	37.203	1.50	0.05169	1.03	37.203	1.50	0.05169	1.03	271.7	23.5	178.0	3.0	171.0	2.5	170.5	2.5	481	84	14	0.080	{0.61}
YL-KG-513	0.18050	1.94	0.0269	1.56	37.187	1.56	0.04868	1.16	37.097	1.56	0.05058	0.91	132.5	27.0	168.5	3.0	171.1	2.6	171.2	2.6	1183	157	35	0.060	{0.24}
YL-KG-513	0.19505	1.88	0.0270	1.52	36.981	1.52	0.05232	1.10	36.981	1.52	0.05232	1.10	299.2	25.0	180.9	3.1	172.0	2.6	171.4	2.6	437	96	13	0.099	{0.67}
YL-KG-554	0.16757	2.75	0.0256	1.57	39.073	1.57	0.04749	2.26	38.705	1.57	0.05491	1.18	73.8	52.9	157.3	4.0	162.9	2.5	163.3	2.5	597	218	18	0.166	{0.94}
YL-KG-554	0.17852	2.27	0.0259	1.71	38.605	1.71	0.04998	1.49	38.605	1.71	0.04998	1.49	194.2	34.2	166.8	3.5	164.9	2.8	164.7	2.8	269	96	8	0.161	{0.55}
YL-KG-554	0.17534	2.77	0.0262	1.58	38.197	1.58	0.04857	2.28	38.046	1.58	0.05169	1.51	127.3	52.7	164.0	4.2	166.6	2.6	166.8	2.6	258	100	8	0.176	{0.40}
YL-KG-554	0.17512	1.84	0.0262	1.53	38.108	1.53	0.04840	1.02	38.040	1.53	0.04980	0.85	118.9	23.9	163.9	2.8	167.0	2.5	167.2	2.5	1149	879	38	0.347	{0.18}
YL-KG-554	0.18040	2.78	0.0264	1.50	37.910	1.50	0.04960	2.34	37.585	1.50	0.05634	1.14	176.3	53.6	168.4	4.3	167.8	2.5	167.8	2.5	408	71	12	0.079	{0.86}
YL-KG-554	0.17809	2.55	0.0264	1.55	37.905	1.55	0.04896	2.03	37.542	1.55	0.05649	1.26	145.8	46.9	166.4	3.9	167.9	2.6	168.0	2.6	773	133	22	0.078	{0.96}
YL-KG-554	0.18302	1.85	0.0266	1.56	37.645	1.56	0.04997	0.99	37.577	1.56	0.05140	0.80	193.6	22.9	170.7	2.9	169.0	2.6	168.9	2.6	988	496	32	0.228	{0.18}
YL-KG-554	0.17744	2.24	0.0266	1.50	37.637	1.50	0.04843	1.66	37.453	1.50	0.05228	0.91	120.6	38.6	165.9	3.4	169.0	2.5	169.3	2.5	665	258	21	0.176	{0.49}
YL-KG-554	0.17962	2.24	0.0266	1.51	37.547	1.51	0.04891	1.65	37.437	1.51	0.05121	1.21	143.7	38.3	167.7	3.5	169.4	2.5	169.6	2.5	465	106	14	0.103	{0.29}
YL-KG-554	0.17722	2.05	0.0267	1.50	37.491	1.50	0.04819	1.39	37.389	1.50	0.05034	1.00	108.5	32.5	165.7	3.1	169.7	2.5	170.0	2.5	590	151	18	0.116	{0.27}
YL-KG-554	0.17960	2.81	0.0267	1.54	37.458	1.54	0.04879	2.35	37.359	1.54	0.05088	1.84	137.9	54.4	167.7	4.4	169.8	2.6	170.0	2.6	208	142	7	0.309	{0.26}
YL-KG-554	0.18070	2.26	0.0269	1.53	37.203	1.53	0.04876	1.67	37.115	1.53	0.05063	1.36	136.1	38.8	168.7	3.5	171.0	2.6	171.1	2.6	473	199	15	0.191	{0.24}
YL-KG-554	0.18166	1.83	0.0270	1.51	37.067	1.51	0.04884	1.04	37.026	1.51	0.04971	0.92	140.0	24.3	169.5	2.9	171.6	2.6	171.8	2.6	759	148	23	0.088	{0.11}
YL-KG-554	0.18311	2.09	0.0270	1.54	36.989	1.54	0.04912	1.41	36.941	1.54	0.05013	1.23	153.7	32.8	170.7	3.3	172.0	2.6	172.0	2.6	411	117	13	0.129	{0.13}
YL-KG-554	0.18150	2.14	0.0271	1.60	36.933	1.60	0.04862	1.42	36.933	1.60	0.04862	1.42	129.4	33.1	169.3	3.3	172.2	2.7	172.4	2.7	280	155	9	0.252	{0.46}
YL-KG-554	0.18817	2.18	0.0272	1.52	36.763	1.52	0.05017	1.56	36.670	1.52	0.05215	1.08	203.0	35.9	175.1	3.5	173.0	2.6	172.9	2.6	460	172	15	0.170	{0.25}

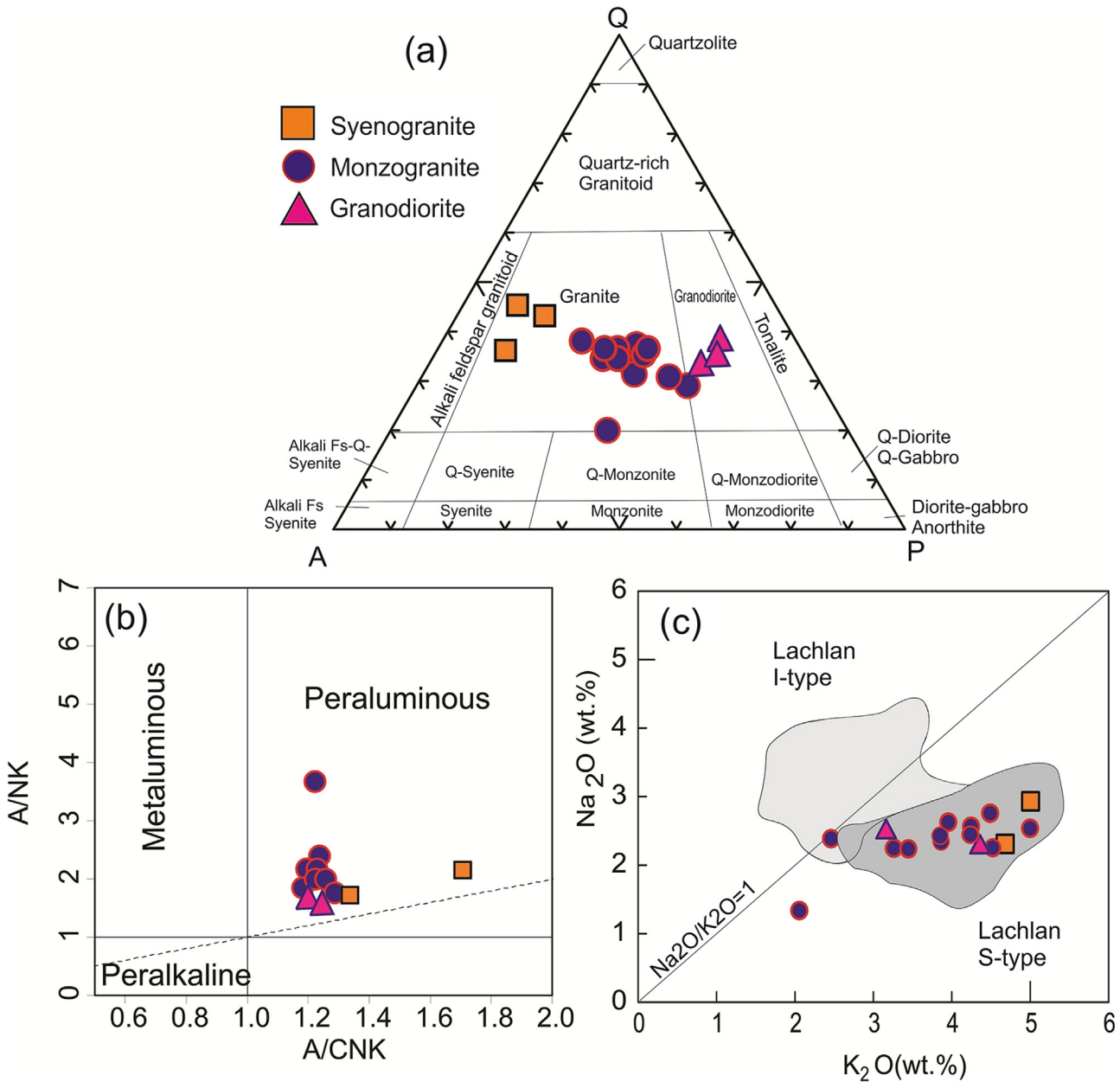

Fig. 7. (a) Quartz-Alkali feldspar-Plagioclase (QAP) classification of KGG samples. (b) Classic A/CNK vs. A/NK diagram of Shand (1943) discriminating metaluminous, peraluminous and peralkaline compositions; (c) Na_2O (wt%) vs. K_2O (wt%) diagram Chappell and White (1983).

5.3.2. Granodiorites (YL-KG-491 and YL-KG-513)

Zircon from two granodiorite samples range in length from 100 to 300 μm, with length to width ratios between 1:1 and 3:1. Most are euhedral and exhibit oscillatory zoning in CL images (Fig. 11b and c). These zircons have U (146–1183 ppm) and Th (36–701 ppm) contents and Th/U ratios of 0.04–0.37. Sixteen and fifteen grains were analyzed from two granodiorite samples (YL-KG-491 and YL-KG-513, respectively). These clusters show the intercept ages of 175.0 ± 2.4 Ma (MSWD = 2.4) and 168.8 ± 1.2 Ma (MSWD = 2.7) (Fig. 12b and c).

5.3.3. Syenogranite (YL-KG554)

Zircons separated from this sample are fine prismatic with abraded pyramids, or are ellipsoidal and are up to 300 μm long (Fig. 11d). Similar to other samples YL-KG513, YL-KG491 and YL-KG374, the CL images show that most zircons in this sample exhibit core–rim structures. Zircons U (208–1149 ppm) and Th (71–879 ppm), and Th/U ratios vary from 0.07 to 0.34 (average 0.17) (Table 8). Eighteen analyzed grains show the intercept age of 169.7 ± 1.2 (MSWD = 1.2) in $^{207}Pb/^{206}Pb$ vs. $^{206}Pb/^{238}U$ diagram (Fig. 12d).

These new zircon U–Pb ages indicate that KGG plutonism lasted from ca. 175 Ma to 167 Ma. It is noteworthy that some zircons show Mesoproterozoic and Paleoproterozoic ages of ca. 1600–1800 Ma, and are clearly inherited.

6. Discussion

Below we discuss some of the implications of our study. First we consider the source of KGG magmas, how the magma evolved, how it crystallized, and what was heat source. Then we compare KGG granitoids with other bodies of similar age in the SNSZ. Finally we consider the implications of our results for reconstructing the Jurassic tectonic setting of the SNSZ.

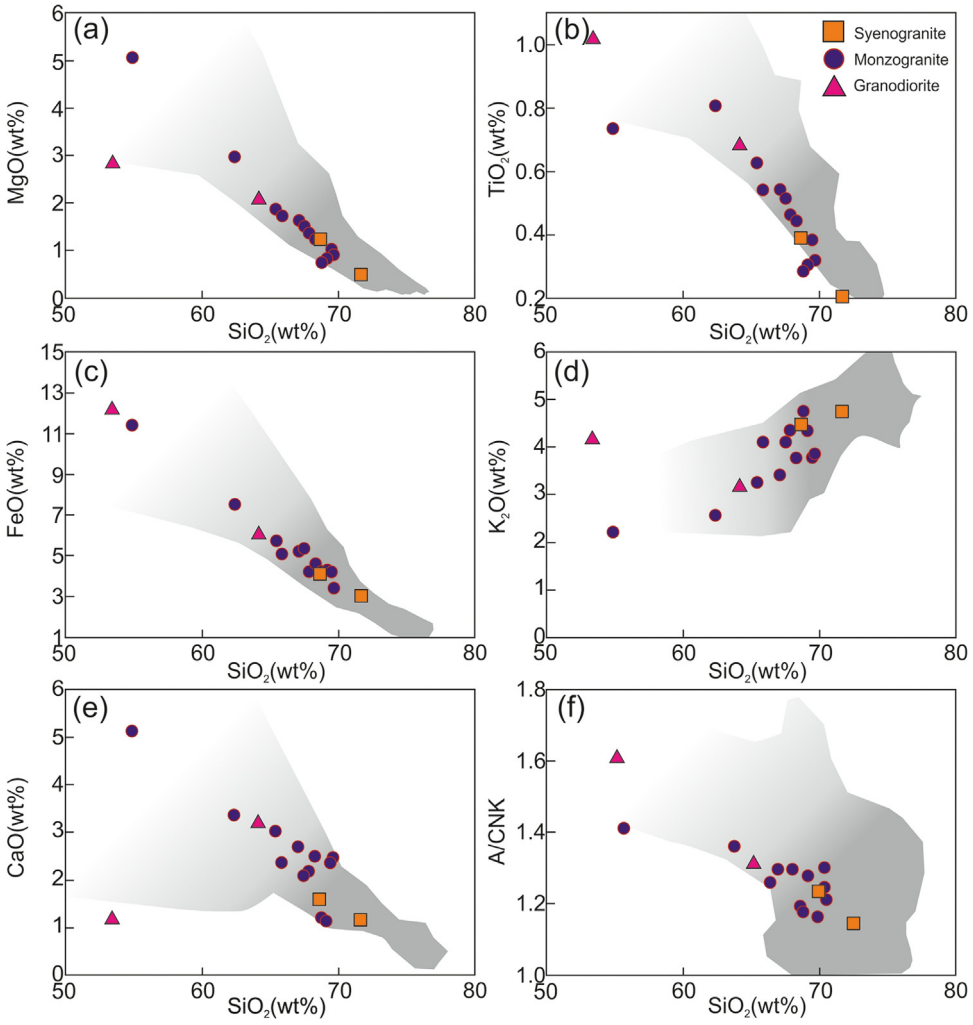

Fig. 8. Variations of major oxides versus SiO_2 for the granitoid rocks from the KGG. Shaded area represent compositional variation within the S-type Cape granite suit (CGS; Villaros et al., 2009), depicted for comparison.

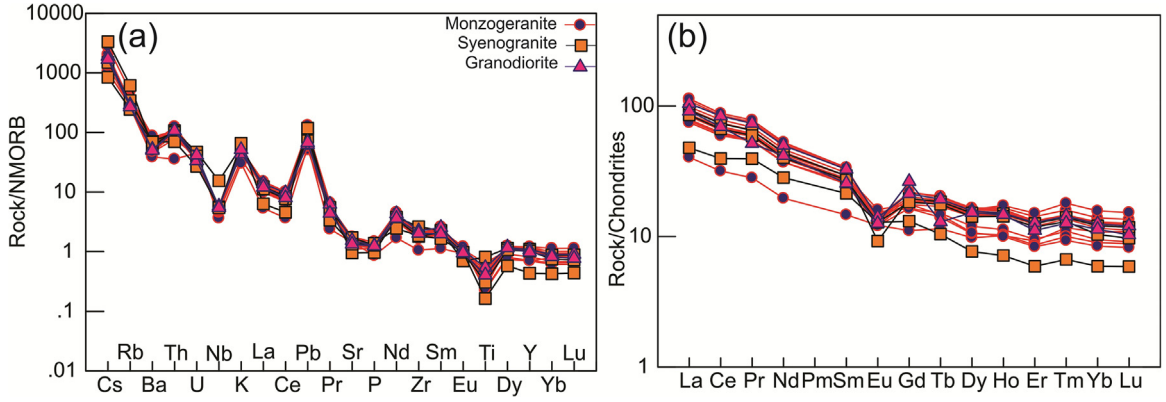

Fig. 9. (a) Primitive mantle normalized trace element spidergrams (after Sun and McDonough, 1989) and (b) Chondrite-normalized REE patterns (Nakamura, 1974) for the KGG.

6.1. Petrogenetic considerations

6.1.1. Magma source

The KGG contain aluminous phases (cordierite, sillimanite, andalusite, garnet) and tourmaline which are unusual in I-type granites but common in S-type granitoids. The KGG geochemical characteristics such as ASI > 1.1 and normative corundum >1% further indicate their peraluminous nature and S-type origin. The trace element characteristics of the KGG include enrichment in incompatible elements (K, Th, Rb, La, Ce, Nd) and depletion in Sr, Ti, P, Ta, Nb, Ba in the N-MORB- and chondrite-normalized diagrams (Chappell and White, 1992). The KGG samples show arc-related trace element signatures including Nb–Ta–Ti depletion and enrichment in Ba, Th, Rb, U, Pb and K (Fig. 9a), although it is not clear how

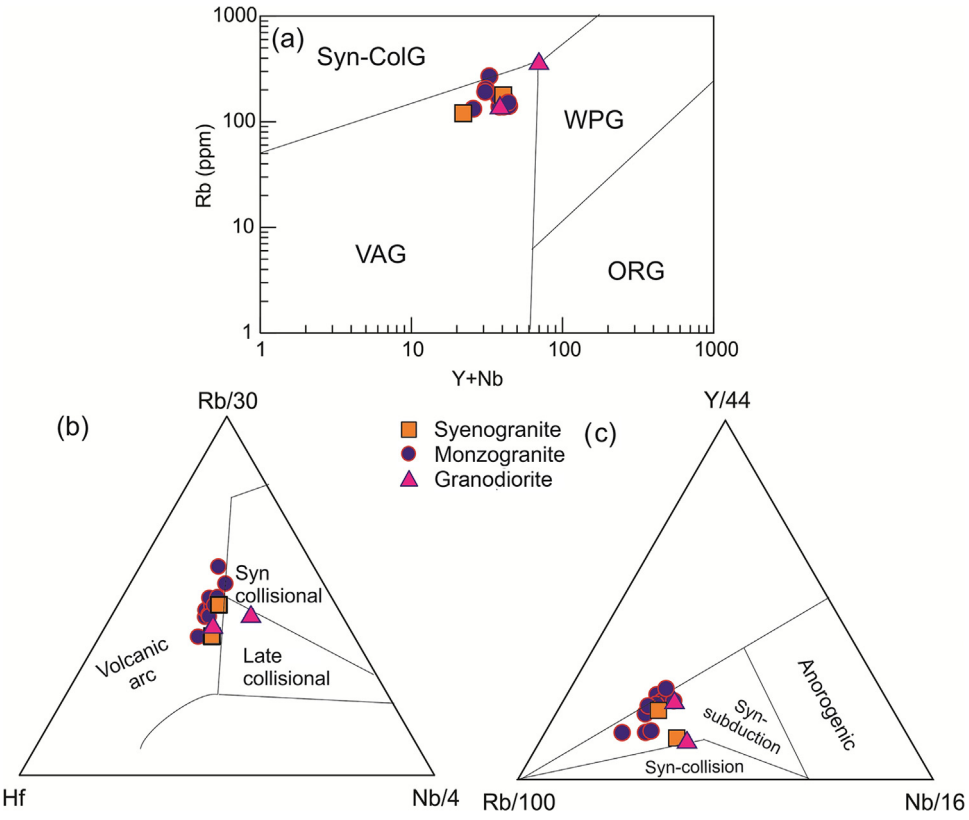

Fig. 10. (a), (b) and (c) Discrimination of granite tectonic setting diagrams; ORG: ocean-ridge granites; syn-COLG: syn- collisional granites; VAG: volcanic arc granites; WPG: within-plate granites. Rb vs. (Y + Nb) diagrams of Pearce et al. (1984); Rb/30-Hf-Nb/4 diagram of Hariss et al. (1986); Y/44, Rb/100, Nb/16 diagram of Thièblemont and Cabanis (1990).

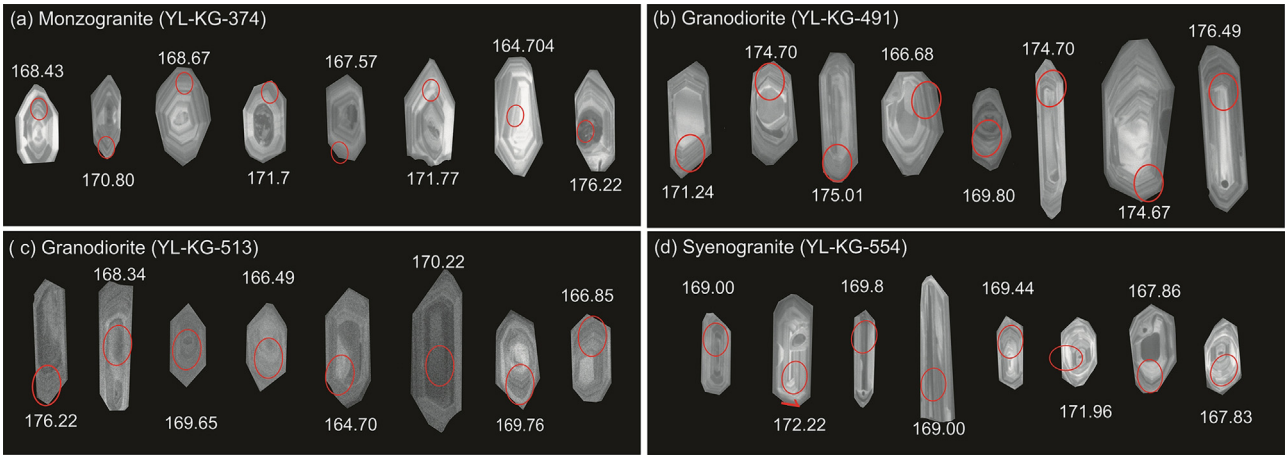

Fig. 11. Cathodoluminescence images of zircon grains in KGG rocks. The circles are analysis spots marked with ages.

much of these characteristics reflect a mantle source and how much is inherited from sedimentary source rocks (Chappell and White, 1974).

Most S-type granites, worldwide, are associated with high-temperature–low-pressure (HTLP) metamorphic complexes, for example in the Buchan area of NE Scotland and Lachlan fold belt, Australia (Cappell and Wayborn, 2012). The absence of high grade regional metamorphic haloes around the KGG testifies to segregation and ascent of magma from the anatectic zone and emplacement along the main Kolah- Ghazi faults. However, the absence of exposed high grade metamorphic rocks in the Kolah-Ghazi region makes it difficult to unequivocally identify the source of KGG magmas. Therefore, it is necessary to utilize multidisciplinary petrological and geochemical evidences to evaluate source region, melting condition, depth of melting and overall magma evolution of the KGG.

It is generally believed that S-type granitic magmas are produced during anatexis from pelitic and/or psammitic rocks in the middle to upper crust (e.g. Osanai et al., 1991). The source of heat and fluids needed to induce partial melting of metasedimentary rocks is debatable. Globally, most S-type granites occur in continent-continent collision zones, where metasedimentary rocks are buried deeply enough to partially melt by thermal relaxation of overthickened crust or heat produced by radioactive decay of U, K, Th bearing minerals (England and Thompson, 1984, 1986). Sources of KGG magmas can be further inferred from experimental

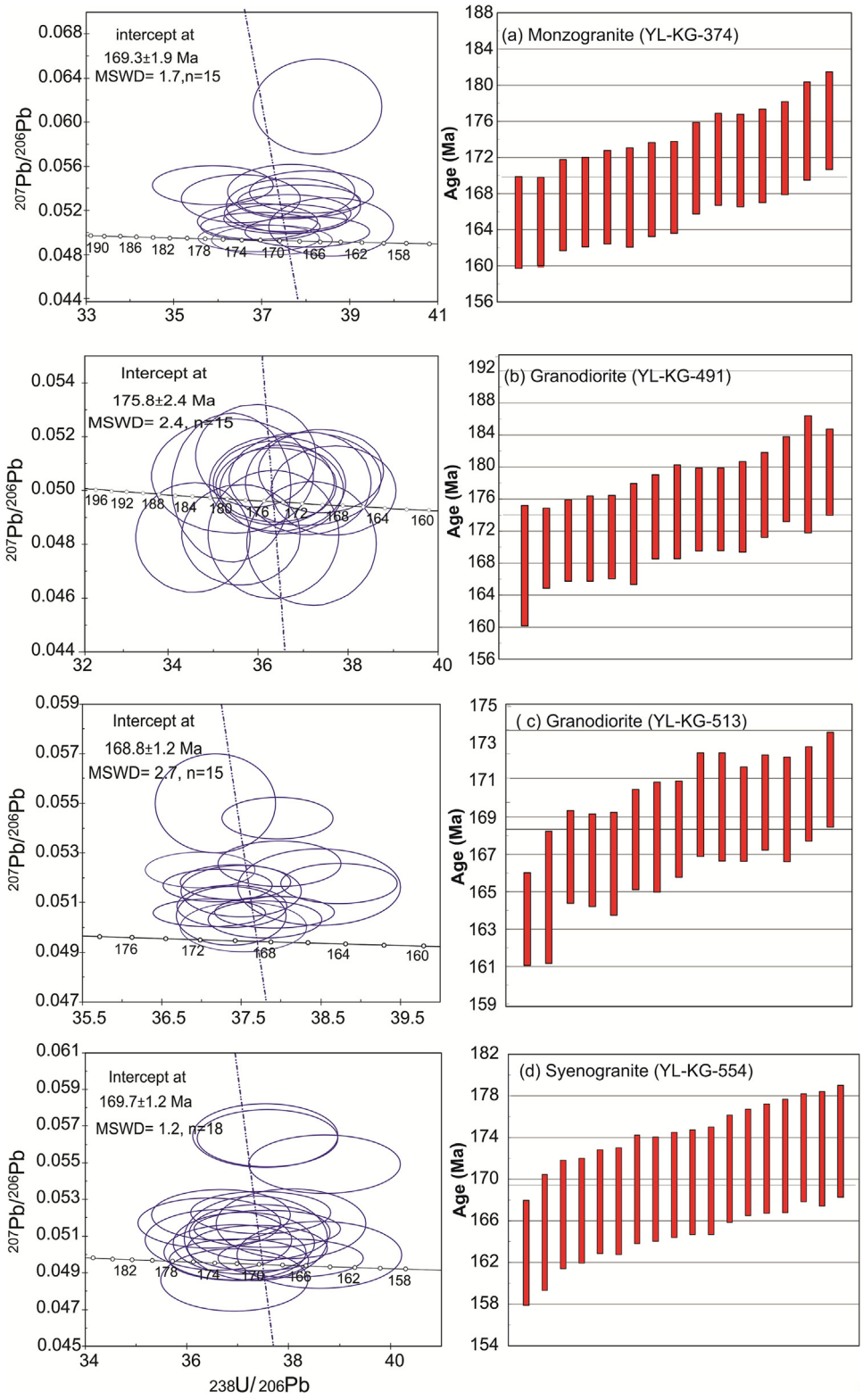

Fig. 12. Intercept age diagram showing zircon U–Pb data for KGG plutonic rocks.

studies on the melting of pelitic, psammitic, andesitic and basaltic rocks. In source discrimination diagrams based on the major and trace elements, most KGG rocks data fall into or near the field for partial melting of metapelites (Fig. 13a–c). In strongly peraluminous granitic melts, Rb, Sr and Ba provide information regarding source rocks and place constraints on the conditions during melting (Miller, 1985; Harris and Inger, 1992). The Rb/Ba vs Rb/Sr plot of Sylvester (1998) has thus been employed to determine the nature of the source rock for the melt (Fig. 13b). This agrees with the suggestion of Sylvester (1998) who stated that S-type peraluminous melts derived from pelites have lower CaO/Na_2O ratios (<0.3) than melts produced from clay-poor (greywacke) sources. Fig. 13c shows the

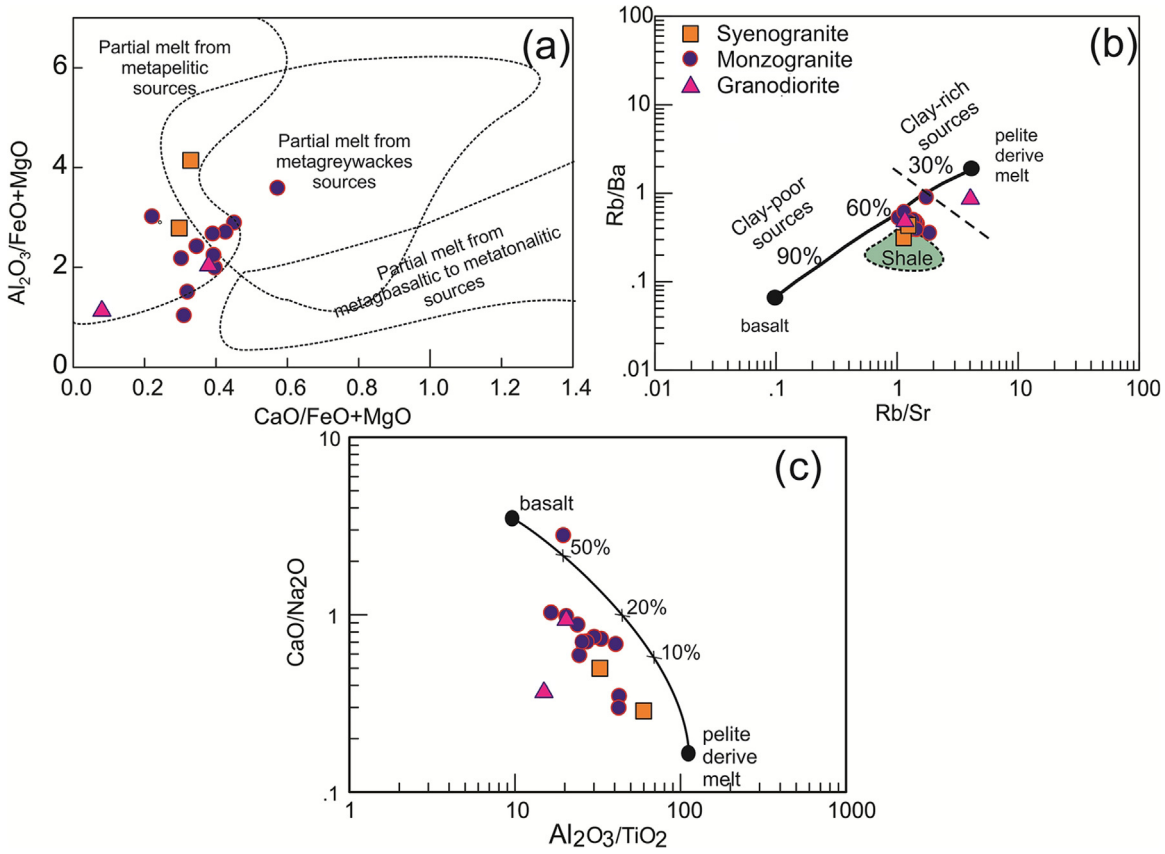

Fig. 13. Source discrimination diagrams for KGG granitoid rocks. (a) After Altherr et al. (2000). (b) and (c) After Sylvester (1998) .

CaO/Na_2O ratios from 0.4 to 1.4 for the KGG rocks; suggests mixed pelitic–greywacke sources.

6.1.2. *The physico-chemical conditions of magma crystallization and source of heat for melting*

The formation temperature of the KGG magmas can be estimated by two methods including: (i) Ti-in-biotite (TIB) geothermometer of Henry et al. (2005) and (ii) Zircon saturation thermometry of Watson and Harrison (1983). The TIB was applied to calculate equilibration temperature of the KGG biotite. The biotite Ti versus Mg/(Mg + Fe) relationships show that biotite from syenogranites and granodiorite crystallized at about 500 °C–550 °C while those from monzogranite crystallized at 550–600 °C (Fig. 14a).

Zircon saturation thermometry of Watson and Harrison (1983) also provides a good estimation of magma temperatures during zircon crystallization. These temperature estimates were calculated using Z (cation ratio (Na + K + 2Ca)/(Al*Si)) from bulk rock compositions. Zr-thermometry illustrates that zircons in the KGG were generated at temperatures ranging from 800 to 850 °C (Fig. 14b). It must be noted that the TIB gives a much lower temperatures than Zr-thermometry (i.e. 500–600 °C vs. 800–850 °C). One explanation for this inconsistency may be that biotite continued to equilibrate at lower temperatures than did zircon. We conclude that KGG magmas were formed at T > 800 °C.

The presence of granulite-facies metamorphism in the lower crust requires temperatures that are higher than normal geothermal gradients, temperature and pressure between 750 and 1000 °C and 2–12 kbar (6–50 km), respectively. The heat required for partial melting of the sediments may have been supplied from several possible sources (Henk et al., 2000): (1) accumulation of radiogenic heat accompanying crustal thickening; (2) burial of highly radioactive rocks; (3) crustal scale shear heating; (4) delamination of lithospheric mantle (Lachenbruch and Sass, 1978; Wickham and Oxburgh, 1985); (5) increased heat flux from the mantle due to asthenospheric upwelling or mantle wedge convection; and (6) emplacement of magma into the crust (e.g. Huppert and Spark, 1988). Many S-type granites also contain MMEs, which could reflect input of mafic, mantle-derived magma into the region of melt generation. The KGG has such enclaves, suggesting that intrusion of mafic mantle-derived magma played an important role (Huppert and Spark, 1988). Another mechanism of crustal melting beneath Andean margins includes channelized upward intrusion of mafic magma into the crust below a volcanic arc (Laube and Springer, 1998). The mafic channels heat the surrounding crust and water released from cooling magma and metamorphosed crust forms a region of partial melting around the conduit zone. Anatexis of metasediments is mainly controlled by biotite breakdown reactions, with heat supplied from mafic magma. This is the most likely source of heat for melting of the KGG source region, as evident by the presence of the MMEs.

In summary, KGG magma were derived from partial melting of metapelite and metagreywacke ~30 km deep in the crust under low water-vapor pressures (0.5-1 Kbar) and ~800 °C. A significant input of mafic mantle-derived magma was also important in their formation.

6.2. *Temporal and spatial comparison of KGG granitoids with other Sanandaj-Sirjan magmatic rocks of Jurassic age*

An important useful perspective on the evolution and genesis of the KGG is to compare it to other Jurassic granitoids found elsewhere in the SNSZ (Fig. 1; Table 9). There are no major differences between Jurassic intrusive rocks of the SNSZ in terms of

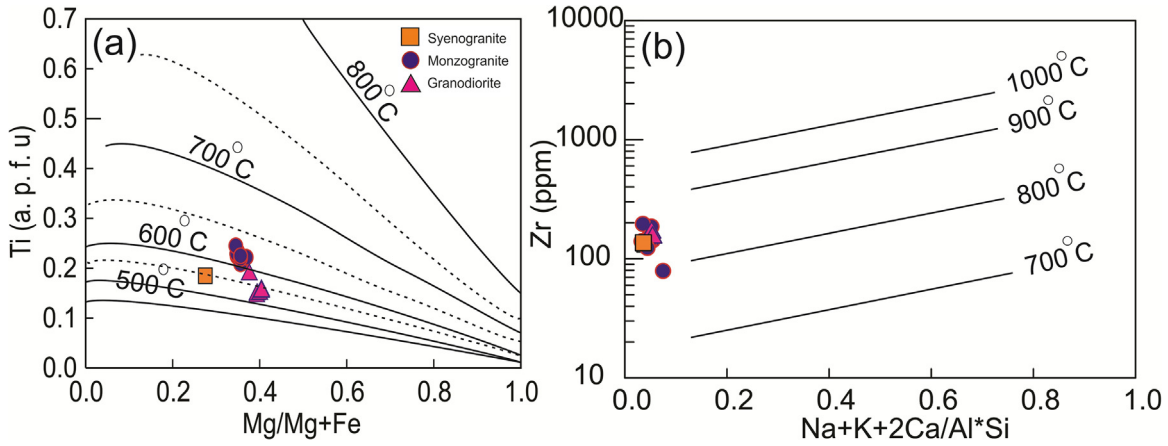

Fig. 14. (a) Ti vs. Mg/ (Mg + Fe) for biotite (after Henry et al., 2005); (b) Cation ratio (Na + K + 2Ca)/(Al*Si) vs. Zr diagram of Watson and Harrison (1983). Symbols as in Fig. 6.

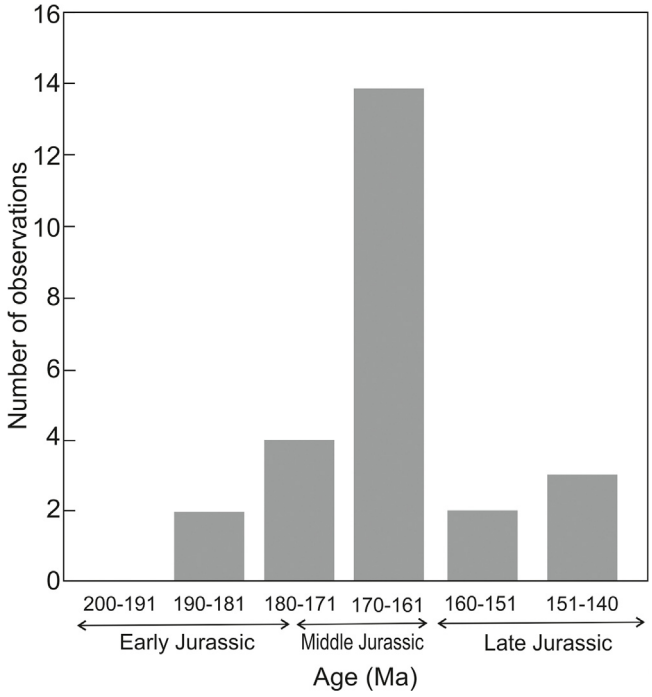

Fig. 15. Jurassic intrusions in the Sanandaj-Sirjan zone (Gr: Granite; Grd: Granodiorite; Mo: Monzonite; Gb: Gabbro: SYG: Syenogranite; Mog: Monzogranite; Qd: Quartz-diorite; To: Tonalite).

ages and rock-type series except for Sr–Nd isotope data indicating different contributions of crust and mantle melts in their genesis (Esnaashari et al., 2012; Ahadnejad et al., 2011; Azizi et al., 2011; Mahmoudi et al., 2011; Shahbazi et al., 2010; Sepahi, 2008; Valizadeh and Cantagrel, 1975). SNSZ magmatism occurred during almost the entire Jurassic (186–144 Ma), with peak activity in Middle Jurassic ~165 Ma (Fig. 15; Table 9). This suggests that all these intrusive bodies are the result of an important magmatic pulse that occurred during Jurassic time in response to the subduction of Neo-Tethyan oceanic crust beneath Iran. The strong folding, magmatism and uplift of the Central Iranian micro-continent and SNSZ in Middle Jurassic time coincides with the middle Cimmerian orogeny and testifies to active subduction of Neo-Tethyan oceanic lithosphere beneath the SNSZ. Most Jurassic granitoids in the SNSZ are calc-alkaline I-types, varying in composition from quartz diorite to monzogranite, and were emplaced above active subduction zones between 176 and 145 Ma, as summarized in Table 9 and as shown in Fig. 15.

Jurassic magmatic rocks of the SNSZ vary from mafic to felsic and from gabbro to syenogranite (Fig. 15). Granitoids with Early Jurassic U–Pb zircon ages are found in the central and southern SNSZ such as the Malayer region (Ahadnejad et al., 2011), and in the Kolah-Ghazi region (this study; Table 9). Late Jurassic plutonic rocks (143 ± 2.3 Ma; Azizi et al., 2011; 149.3 ± 0.2 Ma; Mahmoudi et al., 2011; 144 ± 17 Ma; Valizadeh and Cantagrel, 1975) with I-type characteristics are found in the Suffi Abad and Gorveh plutonic complex and Almagholagh diorites, respectively. Compared to the northern SNSZ, middle Jurassic igneous rocks from the central and southern SNSZ show stronger crustal signatures with less mantle input, with $\varepsilon Nd_{(t)}$ values from −2.3 to −6.0 (Table 9), whereas granitoids from the northern SNSZ show larger mantle inputs, with $\varepsilon Nd_{(t)}$ values from −4.5 to +4.9.

KGG and Shir Kuh granitoid are unlike most Jurassic SNSZ intrusions in having S-type features. Both massifs intruded the Jurassic metasediments and partially melted them. Both S-type granitic bodies are restricted to areas in the southern SNSZ where thick sequences of Jurassic sediment of the Shemshak formation were deposited.

6.3. Tectonic setting and implications for geodynamic evolution

Peraluminous magmas, derived from the partial melting of metasedimentary rocks, are thought to form S-type granites in the continent-continent collision zones (e.g. Chappell and White, 1974, 1992). However, several reported S-type granites are unrelated to collision zones as they are intruded in arc environments (e.g. circum-Pacific plutonic terrane; Collins and Richards, 2008). This seems to be the tectonic environment of KGG and other SNSZ Jurassic granitic rocks, as inferred from trace element discrimination diagrams (Fig. 11) that show that the S-type KGG rocks plot in the volcanic arc granites and syn-subduction fields.

The requirements for source regions suitable for accumulating thick piles of sediments and melting them in an arc-related environment is the subject of considerable debate. The most likely convergent margin settings where thick sections of sediments can accumulate are extensional environments on the overriding plates such as back-arc basins. In an attempt to address the question of why some S-type granites form in convergent margin environments, Collins and Richards, (2008) proposed a plausible multistage process including trench rollback accompanied by crustal extension and back arc basin opening and filling with turbidites followed by flat subduction. Flat subduction led to backarc compression and structural thickening of back-arc turbidite deposits on the overriding plate. The sequence ends with a second episode of trench rollback, resulting in renewed extension and magmatism and con-

Table 9
Jurassic intrusions in the Sanandaj-Sirjan zone.

Number on Map	Name	Composition $ type	Age	Method	Isotopic constraint	Distictive mineralogy	References
1.SUG	Suffi Abad granite	Granite, **I & A**	147.5±1.3 Ma 143.5±2.3 Ma	U-Pb, zircon	($^{87}Sr/^{86}Sr)_i$ =0.7024–0.7069 , $\varepsilon Nd_{(t)}$ = (+1.5 & +4.9)	Hornblende-magnetite	Azizi et al., 2011
2.GPC	Gorveh plutonic complex	-Granite, **I** -Monzonite -Gabbro	156.5±0.6 Ma 151±0.2 Ma 149.3±0.2 Ma	U-Pb, zircon		Amphibole	Mahmoudi et al., 2011
3.AD	Almagholagh diorites	Diorite	144 ± 17 Ma	Rb-Sr in biotite	- ($^{87}Sr/^{86}Sr)_i$= 0.708		Valizadeh and Cantagrel., 1975
4.ALD	Alvand plutonic complex	**1-** Leucocratic granitoids	154.4 ± 1.3 153.3 ± 2.7	U-Pb, zircon	**1-** ($^{87}Sr/^{86}Sr)_i$=(0.713-0.714), $\varepsilon Nd(t)$ =(_3.5 to _4.5).	Tourmaline and kyanite	Mahmoudi et al., 2011 &
		2-Granite**, A** (Shahbazi) S, I	163.9±0.9 Ma 161.7±0.6 Ma		**2-**($^{87}Sr/^{86}Sr)_i$= (0.707–0.719). $\varepsilon Nd(t)$ = (-1.0 to -3.4).		Shahbazi et al., 2010.
		3- Gabbro	166.5±1.8 Ma		**3-** ($^{87}Sr/^{86}Sr)_i$=(0.70230.7037), $\varepsilon Nd_{(t)}$ = (+2.9 to +3.3).		Sepahi.,2008
5.MAG	Malayer granitoids	**1-** Granodiorite,	187±6 Ma 170±4 Ma	U-Pb, zircon	**1-**($^{87}Sr/^{86}Sr)_I$= 0.70855-0.70921. $\varepsilon Nd_{(t)}$ = (-2.7, -3.7).		Ahadneja et al., 2011
		2-Monzogranite, **I**	174±6 Ma 162±8 Ma		2-(87Sr/86Sr)I =0.70797. εNd(t)= -4.9.		
		3-Syenogranite	183±5 Ma 174±5 Ma		**3-**($^{87}Sr/^{86}Sr)_i$ =0.70944. $\varepsilon Nd_{(t)}$ = -3.4.		
		4-Tonalite	169±8 Ma		**4-**($^{87}Sr/^{86}Sr)_i$=0.70877, $\varepsilon Nd_{(t)}$ = -2.3.		
		5-Quartz diorite	172±2 Ma		**5-**($^{87}Sr/^{86}Sr)_i$=0.70856. $\varepsilon Nd_{(t)}$= -2.7		
6.BG	Boru5jerd granitoid	**1-**Quartz-diorites	169.0±1.0 Ma 169.0±0.3 Ma	U-Pb, zircon	**1-** ($^{87}Sr/^{86}Sr)_i$ = 0.7062–0.7074. $\varepsilon Nd_{(t)}$= (-3.62, -3.14)	Amphibole	Mahmoudi et al., 2011 Karimpour
		2-Granodiorite, **I**			**2-** ($^{87}Sr/^{86}Sr)_i$ = 0.7066, $\varepsilon Nd_{(t)}$= (-3.33, -3.53).		
		3-Monzogranite			**3-** ($^{87}Sr/^{86}Sr)_i$ = 0.7063. $\varepsilon Nd_{(t)}$=(-3.02).		
7.ASG	Astaneh granitoid	**1-**Granodiorite	167.5±1.0 Ma	U-Pb, zircon	**1-**($^{87}Sr/^{86}Sr)_i$ = 0.70824- $\varepsilon Nd_{(t)}$ =(-5.8).		Mahmoudi et al., 2011. Karimpour
		2-Quartzdiorite			**2-**($^{87}Sr/^{86}Sr)_i$= 0.70804,0.70842, $\varepsilon Nd_{(t)}$=(-5.6 , -6).		
8.ALG	Aligudarz granitoid	**1-**Quartz-diorites, **2-**Granodiorites, **I** -Granites	164±5.0 Ma 165 ±5.0 Ma	U-Pb, zircon	**1-**($^{87}Sr/^{86}Sr)_i$=0.7074–0.7082, $\varepsilon Nd_{(t)}$ =(-4.8 to -3.6).	Amphibole, magnetite	Esnaashari et al., 2012
					2-($^{87}Sr/^{86}Sr)_i$= 0.7097- 0.7101, $\varepsilon Nd(t)$ = (-5.4, -4.8, -5.5)		
9.DG	Dehbid granite	Granite	Upper Jurassic (See text)	-			Taraz.,1974
10.BMG	Bounin-Miyandasht	Granodiorite, **I**	Upper Jurassic (See text)	-			Sabeti et al., 2012
11.KGG	Kolah-Ghazi granitoid	**1-**Granodiorite	**1-**174.3±1.5 Ma **2-**175±2.4 Ma **3-**170±1.4 Ma	U-Pb, zircon	**1-**10.34, **2-**10.39 **3-**10.57, 9.80		This study
		2-Monzogranite, **S** **3-**Syenogranite 4- Granite	**2-**169.3±1.9 Ma **3-**169.7±1.2 Ma 4-164.6±2.1 & 175.2±1.8 Ma				4- Zarrinkoub, M.H., 2013
12.CDC	ChahDozdan batholith	Granit, **S**	164.3±8.1 Ma	U-Pb, zircon		Ilmenite, Cordierite, gaenet	Fazlnia et al., 2007
13.CBG	ChahBazorgan gabbro	-Gabbro, -Anorthosite, Troctolite, Clinopyroxenite, Wehrlite	170.5 ± 1.9 Ma	U-Pb, zircon		Amphibole	Fazlnia et al., 2013

sequent crustal anatexis to produce S-type granites. This scenario provides a plausible way to generate S-type granitic magmas above subduction zones independent of continental collision. Therefore, the geodynamic evolution of the KGG in the SNSZ is summarized as follows:

During Late Triassic to Middle Jurassic time, the SNSZ was an active Andean-like margin characterized by calc-alkaline magmatism and HP/LT metamorphism in the Shahre-kord area and HT/LP metamorphism in the Sirjan region (Qori complex; Berberian and Berberian, 1981). Moreover, subduction was associated with extension and development of a retro-arc and back-arc basin (e.g. Esfandagheh, Sikhoran, Soghan mafic-ultramafic complex) and several fault-bounded trenches parallel to the central Iranian plateau. Esfandagheh mafic- ultramafic complex and other backarc basins in the Kahnuj region mark the earliest stages of arc retreat and backarc basin opening in Late Triassic to Early Jurassic time (Shafaii Moghadam et al., 2009). Ghasemi and Talbot (2006) believe that the Triassic Sikhoran mafic-ultramafic complex, the Upper Triassic tuff and andesite-basaltic lava flows in the Abadeh area, the mafic-ultramafic rocks of the western Sirjan and the Jurassic tuff

and andesite–basaltic lavas flows, together with some silicic volcanism in the Hajiabad and Dehbid areas, could all be considered as asymmetric magmatic activity in an active margin of the central Iranian plateau along the South Sanandaj–Sirjan Zone due to the opening of a narrow; transtensional Nain–Baft Ocean during Triassic to Jurassic time (Ghazi et al., 2012; Ghazi and Moazzen, 2015).

Extension accompanying arc magmatism filled Late Triassic-Middle Jurassic back-arc basins with thick siliciclastic deposits of the Shemshak Group. Shemshak Group sediments cover most of the SNSZ and have undergone variable grades of metamorphism. Hamadan phyllites are part of this metamorphic sequence and are exposed in belt that is at least 400 km long and 10–100 km wide between the cities of Hamadan and Golpayegan in the northern SNSZ (Stöcklin and Setudehnia, 1991; Mohajjel et al., 2003). In the Esfahan and Kolah-Ghazi regions, a 2500 m thick sequence of Shemshak Group was deposited in a NW-trending basin, termed the Chaleh Syah graben by Zahedi (1976). This sedimentary trough was 25 km wide and over 300 km long, filled by thick flysch type sediment of late Norian to Jurassic (Zahedi, 1976; Thiele et al., 1967).

The Shemshak Group is evidence of not only postcollisional but also synorogenic sedimentation of the Cimmerian orogeny and the onset of Neo-Tethyan back- arc rifting in northern Iran (Zanchi et al., 2009a,b). Detrital zircon geochronology from Shemshak Group sandstone in the southern SNSZ gives U–Pb age clustering at 191 ± 12 Ma (Mousivand et al., 2011). This suggests that the Jurassic arc was the main source area of Shemshak Group sediments in the southern SNSZ. Detrital zircon ages also imply that subduction-related magmatism probably began as early as the Early Jurassic, despite the fact that no such age has been obtained from any SNSZ magmatic rock.

The mid-Cimmerian orogeny in Middle Jurassic time was the main episode of SNSZ magmatism as well as for the entire Central Iranian Plateau (Seyed-emami et al., 2004; Aghanabati, 2004; Fürsich et al., 2009). The Middle Jurassic in the SNSZ is characterized by the termination of Shemshak Group deposition, evident by the regional angular unconformity between these deposits and younger formations, and emplacement of subduction-related plutons, mainly I-type together with some S-type granites. This is, in fact, the time during which metasedimentary rocks buried in the deep crust experienced anatexis and produced mid Jurassic S-type granites such as KGG and Shirkuh granitoid (Aghanabati, 2004; Fürsich et al., 2009; Sheibi et al., 2010).

Moreover, oblique convergence (McClay et al., 2004a,b; Berberian and King, 1981; Shafaii Moghadam, 2009) and subduction of Neo-Tethyan in Mesozoic times caused significant strain partitioning and transpression along and across the SNSZ, forming major ductile to brittle, lithospheric scale extensional shear zones (Mohajjel et al., 2003). Dextral and vertical displacement along these shear zones and faults allowed segregation of melt from the anatectic zone, as evidenced by exposure of KGG along the main northern and southern Kolah-Ghazi range faults. Buoyancy-driven magma ascent and infilling of en-echelon gashes parallel to the northern and southern faults of the Kolah-Ghazi ranges started with granodiorites, followed by monzogranites and ended with syenogranites and aplitic dykes.

Acknowledgments

Authors are very grateful to Y. Vesali for many useful suggestions and encouraging comments on the early version of the paper which greatly contributed to improving the manuscript. Dr. F. Rossetti and an anonymous reviewer of Chemie der Erde journal are also thanked for their invaluable and constructive comments on the final version of the paper. This work was supported by the "Strategic Priority Research Program (B)" of the Chinese Academy of Sciences (grant no. XDB03010800). This study is a part of the Ph.D. thesis by the first author.

References

Abdel-Rahman, A.M., 1994. Nature of biotites from alkaline, calc-alkaline, and peraluminous magmas. J. Petrol. 35, 525–541.
Aghanabati, A., 2004. Geology of Iran. Geological Survey of Iran Publication, Tehran (in Persian).
Aghazadeh, N., Mogaddam, A.A., 2010. Assessment of groundwater quality and its suitability for drinking and agricultural uses in the Oshnavieh area, Northwest of Iran. Journal of Environmental Protection 1 (01), p.30.
Ahadnejad, V., Valizade, M., Deevsalar, R., Rezaei- kahkhaei, M., 2011. Age and geotectonic position of the Malayer granitoids: implication for plutonism in the Sanandaj–Sirjan zone, Western Iran. N. Jb. Geol. Palaont. Abh. 261/1, 61–75.
Ahmadi Khalaji, A., Esmaeily, D., Valizadeh, M.V., Rahimpour-Bonab, H., 2007. Petrologyand geochemistry of the granitoid complex of boroujerd, sanandaj–sirjan Zone,Western Iran. J. Asian Earth Sci. 29, 859–877.
Alavi, M., 1994. Tectonics of the Zagros orogenic belt of Iran: new data and interpretations. Tectonophysics 229 (3–4), 211–238.
Alirezaei, S., Hassanzadeh, J., 2012. Geochemistry and zircon geochronology of the Permian A-type Hasanrobat granite, Sanandaj–Sirjan belt: a new record of the Gondwana break-up in Iran. Lithos 151, 122–134.
Altherr, R., Holl, A., Hegner, E., Langer, C., Kreuzer, H., 2000. High-potassium, calc-alkaline I-type plutonism in the european variscides: northern vosges (France) and northern schwarzwald (Germany). Lithos 50, 51–73.
Arfania, Shahriari, S., 2009. Role of southeastern Sanandaj–Sirjan zone in the tectonic evolution of zagros orogenic belt, Iran. Isl. Arc 18, 555–576.
Azizi, H., Asahara, Y., Mehrabi, B., Chung, S.L., 2011. Geochronological and geochemical constraints on the petrogenesis of high-K granite from the Suffiabad area Sanandaj-Sirjan Zone, NW Iran. Chemie der Erde/Geochemistry 71, 363–376.
Bagherian, S., Khakzad, A., 2001. Petrogenesis of granitoid massif of Molataleb area (north Aligudarz).
Baharifar, A.A., p. 218 (in Persian) 2004. Petrology of Metamorphic Rocks in the Hamedan Area (Doctoral Dissertation, Ph. D Thesis). Tarbiat Moallem University, Tehran, Iran.
Barbero, L., Villaseca, C., 1992. The Layos granite, Hercynian complex of Toledo (Spain): an example of parautochthonous restite-rich granite in a granulitic area. Trans. R. Soc. Edinb. Earth Sci. 83, 127–138.
Berberian, M., King, G.C.P., 1981. Toward a paleogeography and tectonic evalution of Iran. Can. J. Earth Sci. 5, 101–117.
Bouloton, J., 1992. Mise en évidence de cordiérite héritée des terrains traversés dans le pluton granitique des Oulad Ouaslam (Jebilet, Maroc). Can. J. Earth Sci. 29, 658–668.
Chappell, B.W., White, A.J.R., 1974. Two contrasting granite types. Pac. Geol. 8, 173–174, Society of Edinburg, Earth Sciences 8 3:1–26.
Chappell, B.W., White, A.J.R., 1992. I-and S-type granites in the Lachlan Fold Belt. Geol. Soc. Am. Special Papers 272, 1–26.
Chiou, H.Y., Chung, S.L., Zarrinkoub, M.H., Mohammadi, S.S., Khatib, M.M., Iizuka, Y., 2013. Zircon U–Pb age constraints from Iran on the magmatic evolution related to Neotethyan subduction and Zagros orogeny. Lithos 162–163, 70–87.
Claoué-Long, J., Compston, W., Roberts, J., Fanning, C.M., 1995. Two carboniferous ages: a comparison of SHRIMP zircon dating with conventional zircon ages and 40Ar/39Ar analysis. In: Berggren, W.A., Kent, D.V., Aubry, M.P., Hardenbol, J. (Eds.), Geochronology, Time Scales and Stratigraphic Correlation, vol. 54. SEPM Special Publication, pp. 1–22.
Clarke, D.B., 1995. Cordierite in felsic igneous rocks: a synthesis. Mineral. Mag. 59, 311–325.
Davoudian, A.R., Khalili, M., Noorbehsht, I., Dachs, E., Genser, J., Shabanian, N., 2006. Geochemistry of metabasites in the north of the Shahrekord, Sanandaj-Sirjan Zone, Iran. Neues Jahrbuch für Mineralogie-Abhandlungen: J. Mineral. Geochem. 182 (3), 291–298.
Davoudian, A.R., Genser, J., Daches, E., Shabanian, N., 2007. Petrology of eclogites from north of Shahrekord, Sanandaj- Sirjan Zone, Iran. Mineral. Petrol. 92, 393–413.
Davoudzadeh, M., Schmidt, K., 1984. A review of the Mesozoic paleogeography and paleotectonic evolution of Iran. Neues Jahrbuch für Geologie und Paläontologie. Abhandlungen 168 (2/3), 182–207.
Eftekharnejad, J., 1981. Tectonic division of Iran with respect to sedimentary basins. J. Iran. Petrol. Soc. 82, 19–28.
England, P.C., Thompson, A.B., 1984. Pressure-Temperature-Time paths of regional metamorphism I. Heat transfer during of regions of thickened continental crust. J. Petrol. 25, 894–928.
England, P.C., Thompson, A.B., 1986. Some thermal and tectonic models for crustal melting in continental collision belts, in collision tectonics, edited by M.P. Coward and S. C. Ries. Spec. Publ. Geol. 39, 279–296.
Fürsich, F.T., Wilmsen, M., Seyed- Emami, K., Majidifard, M.R., 2009. Lithostratigraphy of the Upper Triassic–Middle Jurassic Shemshak Group of Northern Iran. Geol. Soc. Lond. Spec. Publ. 312 (1), 129–160.

Fazlnia, A.N., Schenk, V., Van der Straaten, F., Mirmohammadi, M.S., 2009. Petrology, geochemistry, and geochronology of trondhjemites from the qori complex, Neyriz, Iran. Lithos 112, 413–433.
Foster, M.D., 1960. Interpretation of composition of trioctahedral micas. U.S. Geol. Surv. Prof. Pap. 354B, 1–49.
Ghasemi, A., Talbot, C.J., 2006. A new tectonic scenario for the Sanandaj–Sirjan Zone (Iran). J. Asian Earth Sci. 26 (6), 683–693.
Ghazi, J.M., Moazzen, M., 2015. Geodynamic evolution of the Sanandaj-Sirjan zone, Zagros Orogen, Iran. Turk. J. Earth Sci. 24 (5), 513–528.
Ghazi, J.M., Moazzen, M., Rahgoshay, M., Moghadam, H.S., 2012. Geochemical characteristics of basaltic rocks from the Nain ophiolite (Central Iran); constraints on mantle wedge source evolution in an oceanic back arc basin and a geodynamical model. Tectonophysics 574, 92–104.
Harris, N.B.W., Inger, S., 1992. Trace element modeling of pelite-derived granites. Contrib. Mineral. Petrol. 110, 46–56.
Henk, A., von Blanckenburg, F., Finger, F., Schaltegger, U., Zulauf, G., 2000. Synconvergent high- temperature metamorphism and magmatism in the Variscides: a discussion of potential heat sources. In: Franke, W., Haak, V., Oncken, O., Tanner, D. (Eds.), Orogenic Processes: Quantification and Modeling in the Variscan Belt, vol. 179. Geological Society London, pp. 387–399 (Special Publications).
Henry, D.J., Guidotti, C.V., Thomson, J.A., 2005. The Ti-saturation surface for lowtomedium pressure metapelitic biotite: implications for geothermometry and Ti-substitution mechanisms. Am. Mineral. 90, 316–328.
Henry, D.J., Novak, M., Hawthorne, F.C., Ertl, A., Dutrow, B.L., Uher, P., Pezzotta, F., 2011. Nomenclature of the tourmaline-supergroup minerals. Am. Mineral. 96, 895–913.
Huppert, H.E., Spark, R.S.J., 1988. The generation of granitic magma by injection of basaltic sill. Trans. R. Soc. Edinb. Earth Sci. 79, 237–243.
Joyce, A.S., 1973. Chemistry of the minerals of the granitic Murrumbidgee batholith, Australian Capital Territory. Chent. Geol. LL, 27l–296.
Khalil, Kh., Khalili, in Persian 2002. The Origin of Kolah-Ghazi Granites and Their Enclaves (SSE of Esfahan), Msc Thesis. University of Esfahan, Esfahan, Iran.
Khosrow-Tehrani, Kh., 1970. Etude stratigraphique du Cretace superieur et du Paleogen de Iran Central. Ph.D. Thesis. Univ. Pierre et Marie Curie, VI, Paris.
Lachenbruch, A.H., Sass, J.H., 1978. Heat flow in the United State and the thermal regime of the crust. In: Heacock, J.K. (Ed.), The Earth's Crust, vol. 20. Amer. Geophys. Union Geophys. Mon., pp. 626–675.
Li, X.H., Sun, M., Wei, G.J., Liu, Y., Lee, C.Y., Malpas, J., 2000. Geochemical and Sm-Nd isotopic study of amphibolites in the Cathaysia Block, southeastern China: evidence for an extremely depleted mantle in the Paleoproterozoic. Precambrian Res. 102, 251–262.
Li, X.H., Qi, C.S., Liu, Y., Liang, X.R., Tu, X.L., Xie, L.W., Yang, Y.H., 2005. Petrogenesis of the Neoproterozoic bimodal volcanic rocks along the western margin of the Yangtze Block: new constraints from Hf isotopes and Fe/Mn ratios. Chin. Sci. Bull. 50, 2481–2486.
Li, Q.L., Li, X.H., Liu, Y., Tang, G.Q., Yang, J.H., Zhu, W.G., 2010a. Precise U-Pb and Pb Pb dating of Phanerozoic baddeleyite by SIMS with oxygen flooding technique. J. Anal. At. Spectrom. 25, 1107–1113.
Li, X.H., Tang, G.Q., Gong, B., Yang, Y.H., Hou, K.J., Hu, Z.C., Li, Q.L., Liu, Y., Li, W.X., 2013. Qinghu zircon: a working reference for microbeam analysis of U-Pb age and Hf and O isotopes. Chin. Sci. Bull. 58, http://dx.doi.org/10.1007/s11434-013-5932-x.
Ludwig, K.R., 2001. User Manual for Isoplot/Ex Rev. 2.49, Special Publication LA. Berkeley Geochronology Center, Berkeley, California.
Mahmoudi, S., Corfu, F., Masoudi, F., Mehrabi, B., Mohajjel, M., 2011. U-Pb dating and emplacement history of granitoid plutons in the northern Sanandaj–Sirjan Zone, Iran. J. Asian Earth Sci. 41, 238–249.
Masoudi, F., 1997. Contact metamorphism and pegmatite development in the region SW of Arak, Iran.
McClay, K.R., Whitehouse, P.S., Dooley, T., Richards, M., 2004. 3D evolution of fold and thrust belts formed by oblique convergence, In: Needham, D.T., Butler, R.W.H., Matthews, S.J., eds., Oil and gas in compressional belts: Marine and Petroleum Geology, vol. 21, pp. 857–877.
McClay, K.R., Whitehouse, P.S., Dooley, T., Richards, M., 2004b. 3D evolution of fold and thrust belts formed by oblique convergence. Mar. Petrol. Geol. 21 (7), 857–877.
Miller, C., 1985. Are strongly peraluminous granites derived from pelitic sedimentary sources? J. Geol. 93, 673–689.
Moazzen, M., Moayyed, M., Modjarrad, M., Darvishi, E., 2004. Azna granitoid as an example of syn-collision S-type granitisation in Sanandaj-Sirjan metamorphic belt Iran. Neues Jahrbuch für Mineralogie-Monatshefte 2004 (11), 489–507.
Mohajjel, M., Fergusson, C.L., 2000. Dextral transpression in Late Cretaceous continental collision, Sanandaj–Sirjan zone, western Iran. J. Struct. Geol. 22 (8), 1125–1139.
Mohajjel, M., Fergusson, C.L., Sahandi, M.R., 2003. Cretaceous–Tertiary convergence and continental collision, Sanandaj–Sirjan Zone, western Iran. J. Asian Earth Sci. 21, 397–412.
Mousivand, F., Rastad, E., Meffre, S., Peter, J.M., Solomon, M., Khin, Z., 2011. U-Pb geochronology and Pb isotope characteristics of the Chahgaz volcanogenic massive sulfide deposit, South of Iran. Int. Geol. Rev. 53 (10), 1239–1262.
Nachit, H., Ibhi, A., Abia, E.H., et al., 2005. Discrimination between primary magmatic biotites, reequilibrated biotites and neoformed biotites. Compt. Rendus Geosci. 337, 1415–1420.
Nakamura, N., 1974. Determination of REE, Ba, Fe, Mg, Na and K in carbonaceous and ordinary chondrites. Geochim. Cosmochim. Acta 38 (5), 757–775.
Nasdala, L., Hofmeister, W.G., Norberg, N., Mattinson, J.M., Corfu, F., Dorr, W., Kamo, S.L., Kennedy, A.K., Kronz, A., Reiners, P.W., Frei, D., Kosler, J., Wan, Y.S., Gotze, J., Hager, T., Kroner, A., Valley, J.W., 2008. Zircon M257 – a homogeneous natural reference material for the ion microprobe U-Pb analysis of zircon. Geostand. Geoanal. Res. 32, 247–265.
Noghreyan, M., Tabatabaei- Manesh, S.M., 1995. A study of Kolah-Ghazi granitoid with emphasize on its contact metamorphism (in Farsi with English abstract). Geosci.Q. GSI 4 (17–18), 60–79.
Omrani, J., Agard, P., Whitechurch, H., Benoit, M., Prouteau, G., Jolivet, L., 2008. Arc-magmatism and subduction history beneath the Zagros Mountains, Iran: a new report of adakites and geodynamic consequences. Lithos 106 (3), 380–398.
Osanai, Y., Komatsu, M., Owada, M., 1991. Metamorphism and granite genesis in the Hidaka metamorphic belt Hokkaido, Japan. J. Metamorphic Geol. 9, 111–124.
Pearce, J.A., Harris, N.W., Tindle, A.G., 1984. Trace element discrimination diagrams for the tectonic interpretation of granitic rocks. J. Petrol. 25, 956–983.
Pereira, M.D., Bea, F., 1994. Cordierite-producing reactions in the Peña Negra Complex, Avila Batholith, Central Spain: the role of cordierite in low-pressure anatexis. Can. Mineral. 32, 763–780.
Pinto, M.M.S.C., 2001. Mineralizações uraníferas no Vale de Abrutigae estudo do impacto ambiental da sua exploração. Unpublished M.Sc. thesis. Univ. Coimbra, 312 pp.
Rachidnejad-Omran, N., 2002. Petrology and Geochemistry of Meta Volcano-sedimentary and Plutonic Rocks of Muteh Area with Special Respect to Genesis of Gold Mineralization, South Delijan, SSW of Tehran, Iran. University of Tarbiat Modares (in Farsi).
Sepahi, A.A., Athari, S.F., 2006. Petrology of major granitic plutons of the northwestern part of the Sanandaj-Sirjan Metamorphic Belt, Zagros Orogen, Iran: with emphasis on A-type granitoids from the SE Saqqez area. Neues Jahrbuch für Mineralogie- Abhandlungen: J. Mineral. Geochem. 183 (1), 93–106.
Sepahi, A., 1999. Petrology of the Alvand Plutonic Complex with Special Reference on Granitoids. PhD. Tarbiat-Moallem University, Tehran, Iran (in Persian).
Sepahi, A.A., 2008. Typology and petrogenesis of granitic rocks in the Sanandaj-Sirjan metamorphic belt, Iran: with emphasis on the Alvand plutonic complex. N. Jb. Geol. Paläont. Abh. 247, 295–312.
Seyed-emami, K., Fursich, F.T., Wikmsen, M., 2004. Documentation and significance of tectonic events in the northern Tabas Block (east-central Iran) during the Middle and Late Jurassic. Rivista Italiana di Paleontologia e Stratigrafia (Res. Paleontol. Stratigr.) 110 (1).
Shafaii Moghadam, H., Stern, R.J., 2011. Late cretaceous forearc ophiolites of Iran. Isl. Arc 20, 1–4.
Shafaii Moghadam, H.S., Stern, R.J., 2015. Ophiolites of Iran: keys to understanding the tectonic evolution of SW Asia: II) Mesozoic ophiolites. J. Asian Earth Sci. 100, 31–59.
Shafaii Moghadam, H., Whitechurch, H., Rahgoshay, M., Monsef, I., 2009. Significance of Nain- Baft ophiolitic belt (Iran): short-lived, transtensional Cretaceous back-arc oceanic basins over the Tethyan subduction zone. Comptes Rendus Geosci. 341, 1016–1028.
Shahbazi, H., Siebel, W., Pourmoafee, M., Ghorbani, M., Sepahi, A.A., Shang, C.K., Vousoughi Abedini, M., 2010. 2010. Geochemistry and U–Pb zircon geochronology of the Alvand plutonic complex in Sanandaj–Sirjan Zone (Iran): New evidence for Jurassic magmatism. J. Asian Earth Sci., http://dx.doi.org/10.1016/j.jseaes.2010.04.014.
Shand, S.J., 1943. Eruptive Rocks, Their Genesis, Composition, Classification, and Their Relations to Ore Deposits. John Wiley & Sons, Inc., New York.
Sheibi, M., Esmaeily, D., Nédélec, A., Bouchez, J.L., Kananian, A., 2010. Geochemistry and petrology of garnet-bearing S-type shir-Kuh granite, southwest yazd, central Iran. Isl. Arc 19 (2), 292–312.
Sheikholeslami, M.R., Pique, A., Mobayen, P., Sabzehei, M., Bellon, H., Emami, M.H., 2008. Tectono-metamorphic evolution of the Neyriz metamorphic complex, Quri-kor-e- sefid area (Sanandaj-Sirjan Zone, SW Iran). J. Asian Earth Sci. 31 (4), 504–521.
Sláma, J., Košler, J., Condon, D.J., Crowley, J.L., Gerdes, A., Hanchar, J.M., Horstwood, M.S.A., Morris, G.A., Nasdala, L., Norberg, N., Schaltegger, U., Schoene, B., Tubrett, M.N., Whitehouse, M.J., 2008. Pleáovice zircon. A new natural reference material for U–Pb and Hf isotopic microanalysis. Chem. Geol. 249, 1–35.
Stöcklin, J., Setudehnia, A., 1991. Stratigraphic lexicon of Iran. Geol. Surv. Iran, 1–376, Rep. 18.
Stacey, J.S., Kramers, J.D., 1975. Approximation of terrestrial lead isotope evolution by a 2- stage model. Earth Planet. Sci. Lett. 26, 207–221.
Streckeisen, A.L., 1973. Plutonic rocks: classification and nomenclature recommended by the IUGS subcommission of the systematics of igneous rocks. Geotimes 18, 26–30.
Sun, S.S., McDonough, W.F.S., 1989. Chemical and isotopic systematics of oceanic basalts: implications for mantle composition and processes. Geol. Soc., London, Spec. Publ. 42 (1), 313–345.
Sylvester, P.J., 1998. Post-collisional strongly peraluminous granites. Lithos 45, 29–44.
Tera, F., Wasserburg, G., 1972. U–Th–Pb systematics in three Apollo 14 basalts and the problem of in itialPb in lunar rocks. Earth Planet. Sci. Lett. 14, 281–304.
Thieblemont, D., Cabanis, B., 1990. Utilisation d'un diagramme (Rb/100)-Tb-Ta pour la discrimination géochimique et l'étude pétrogénétique des roches magmatiques acides. Bull. Soc. Geol. Fr. 6 (1), 23–35.

Valizadeh, M.V., Cantagrel, J.M., 1975. Premières données radiométriques (K–Ar et Rb–Sr) sur les micas du complexe magmatique du mont Alvand, prés d Hamadan (Iran occidental). CR Acad. Sci. Paris Sér. D 281, 1083–1086.
Verdel, C., Wernicke, B.P., Hassanzadeh, J., Guest, B., 2011. A Paleogene extensional arc flare-up in Iran. Tectonics 30 (3).
Villaros, A., Stevens, G., Moyen, J.F., Buick, I.S., 2009. The trace element compositions of S-type granites: evidence for disequilibrium melting and accessory phase entrainment in the source. Contrib. Min. Petrol. 158 (4), 543–561.
Villaseca, C., Barbero, L., 1994. Chemical variability of Al–Ti–Fe–Mg minerals in peraluminous granitoid rocks from Central Spain. Eur. J. Mineral. 6, 670–691.
Watson, E.B., Harrison, T.M., 1983. Zircon saturation revisited: temperature and composition effects in variety of crustal magma type. Earth Planet. Sci. Lett. 64, 295–394.
White, A.J.R., Chappell, B.W., 1977. Ultrametamorphism and granitoid genesis. Tectonophysics 43 (1–2), 7–22.
Zahedi, M., 1976. Explanatory text of Esfahan, Geological Quadrangle Map1:250000, No. F8 Geological Survey of Iran, Tehran.
Zanchi, A., Zanchetta, S., Berra, F., Mattei, M., Garzanti, E., Molyneux, S., Nawab, A., Sabouri, J., 2009a. The Eo-Cimmerian (Late? Triassic) orogeny in North Iran. Geol. Soc. Lond. Spec. Publ. 312 (1), 31–55.
Zanchi, A., Zanchetta, S., Garzanti, E., Balini, M., Berra, F., Mattei, M., Muttoni, G., 2009b. The Cimmerian evolution of the Nakhlak–Anarak area, Central Iran, and its bearing for the reconstruction of the history of the Eurasian margin. Geol. Soc. Lond. Spec. Publ. 312 (1), 261–286.